Stony Brook University

Homogenous and Heterogeneous Ice Nucleation from Biomass Burning Aerosol: Freezing Temperatures and Nucleation Rates

A Thesis Presented by

Yannick J. Rigg

to

The Graduate School

in Partial Fulfillment of the

Requirements

for the Degree of

Master of Science

in

Marine and Atmospheric Science

Stony Brook University

December 2011

Stony Brook University

The Graduate School

Yannick J. Rigg

We, the thesis committee for the above candidate for the
Master of Science degree, hereby recommend
acceptance of this thesis.

Dr. Daniel A. Knopf, Thesis Advisor

Assistant Professor, School of Marine and Atmospheric Science

Dr. Josephine Y. Aller

Professor, School of Marine and Atmospheric Science

Dr. John E. Mak

Associate Professor, School of Marine and Atmospheric Science

This thesis is accepted by the Graduate School

Lawrence Martin

Dean of the Graduate School

Abstract of the Thesis

Homogenous and Heterogeneous Ice Nucleation from Biomass Burning Aerosol: Freezing Temperatures and Nucleation Rates

by

Yannick J. Rigg

Master of Science

in

Marine and Atmospheric Science

Stony Brook University

2011

Biomass burning is a major source of water soluble and water insoluble organic compounds in the atmosphere. These compounds have the potential to form ice via homogeneous and heterogeneous mechanisms, both of which are involved in the formation of cirrus clouds with subsequent effects on the global radiative budget. Aqueous levoglucosan/$(NH_4)_2SO_4$ droplets of mass ratio 10:1, 1:1, 1:5, and 1:10 and aqueous multi component organic droplets with and without $(NH_4)_2SO_4$ serve as surrogates of water soluble organic biomass compounds to be examined for homogeneous ice nucleation. Pahokee Peat and Leonardite serve as surrogates of aerosols composed of HULIS, employed for immersion mode heterogeneous ice nucleation. Homogeneous and heterogeneous freezing and melting temperatures were experimentally obtained for all particle systems over a water activity range of 1.0 - 0.8. Subsequent homogeneous and heterogeneous ice nucleation rates were derived and analyzed based on water activity based theory. Contact angles were derived for the two ice nuclei at atmospherically relevant conditions. Cumulative and differential freezing spectra are calculated from freezing data for the two ice nuclei. Atmospheric implications are also discussed.

Contents

1 Introduction

1.1 Structure of Atmosphere

The Earth's atmosphere is divided into four layers (troposphere, stratosphere, mesosphere, and thermosphere), in which boundaries are defined by the vertical temperature profile as depicted in Figure 1 and where pressure decreases exponentially with height (Wallace and Hobbs, 2006). The first layer, the troposphere, extends from the surface to ∼10 km and has a temperature profile which decreases with increasing height. In the tropics the troposphere extends up to ∼17 km, with temperatures as low as -80°C, whereas in the polar regions the troposphere is bounded at ∼10 km (Wallace and Hobbs, 2006). Tropospheric air contains ∼80% of the mass of the atmosphere. Air is composed of mixture of 78.1% nitrogen (N_2), 20.95% oxygen (O_2), 0.93% argon (Ar), 0-5% water vapor (H_2O), and the remaining percentage is composed of various gases such as CO_2 and Ne (Wallace and Hobbs, 2006).

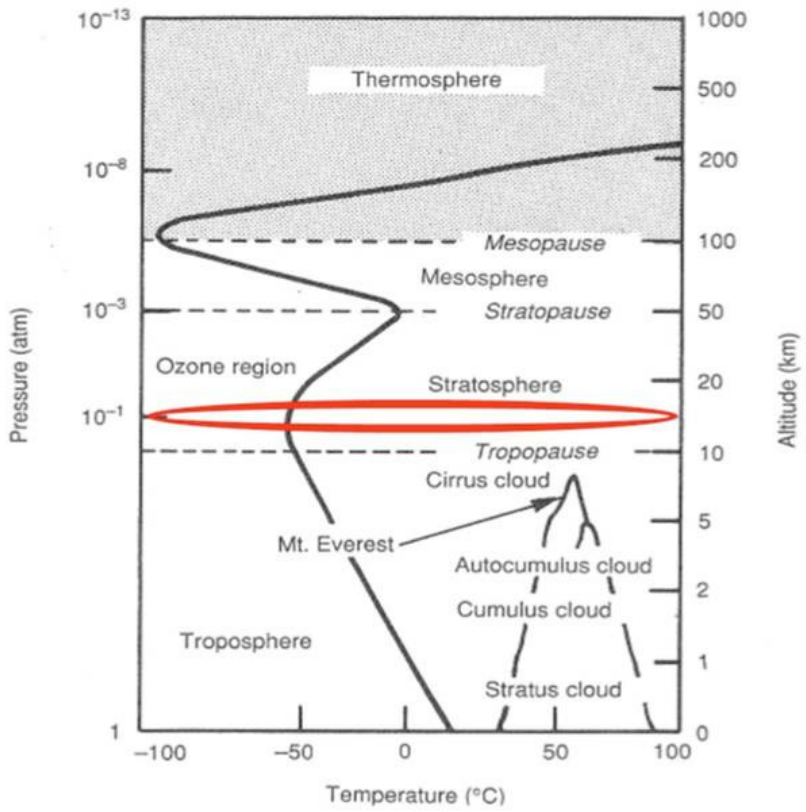

Figure 1: Structure of Earth's atmosphere shown as a function of temperature and pressure.

The second layer of the atmosphere is the stratosphere, which ranges from ∼10 km to ∼50 km and is characterized by an increase in temperature with height. This increase in temperature is because of ozone (O_3) which absorbs ultraviolet (UV) energy waves from the sun and is broken down into atomic oxygen (O) and diatomic oxygen (O_2). These two oxygen species recombine to form O_3, which releases heat and subsequently heats the stratosphere. 99.9% of the mass of the atmosphere is concentrated within the stratosphere and troposphere (Wallace and Hobbs, 2006).

Above this layer is the mesosphere, which extends from ∼50 km to ∼80 km and is defined by a gradual decrease in temperature with height. The final layer in the Earth's atmosphere is the thermosphere which spans from ∼80 km to ∼100 km and defined by an increase in temperature with height. This increase is due to the dissociation of N_2 and O_2 and the removal of electrons from atoms (Wallace and Hobbs, 2006). The temperature within this layer varies in response to emissions in UV and X-ray radiation from the sun (Wallace and Hobbs, 2006). Of all these layers, the troposphere is particularly important as it is the layer in which humans exist in addition to being the crucial reference for global warming studies. In addition to gas phase species in the atmosphere, there are other important species including aerosol particles.

1.2 Aerosol

An aerosol is defined as the suspension of solid and/or liquid matter in a gas, and in the context of the atmosphere, the gas is air. Aerosol particles are ubiquitous in the atmosphere, within a cubic centimeter of air (cm^3) there can be as many as 10^7 particles in urban areas[?] and in an indoor setting there can be as many as 10^5 particles per cm^3 of air (He, et al. 2004). Aerosol particles come in a wide array of shapes and sizes, which depends upon

their source. Two major sources of natural aerosol are soil dust and sea spray (Seinfeld and Pandis, 1998). Anthropogenic aerosol sources include fossil fuel combustion from vehicles and industrial processes and biomass burning (Seinfeld and Pandis, 1998). In addition to primary sources, there are secondary sources of aerosol which arise from chemical reactions involving gas phase species, such as O_3 and biogenic hydrocarbons and can account for up to 20% of the total organic aerosol (Chung and Seinfield, 2002).

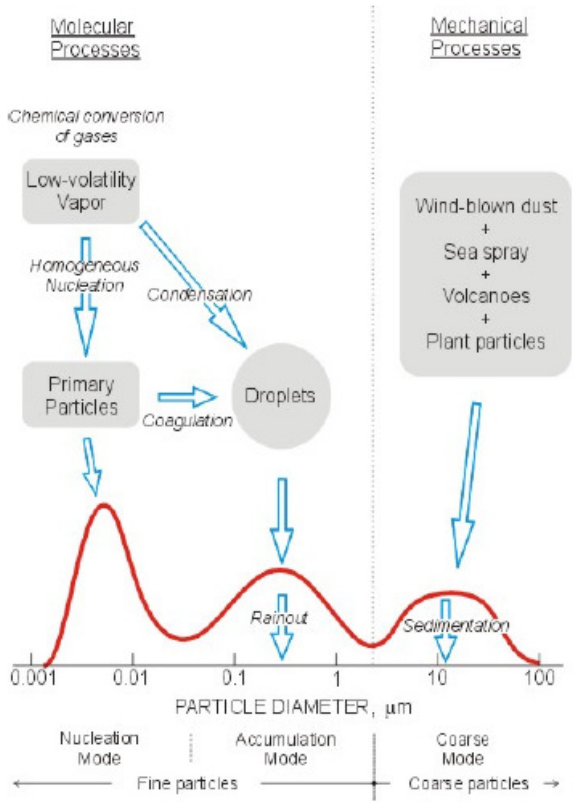

Figure 2: Sketch of atmospheric aerosol formation mechanisms and corresponding trimodal aerosol size distribution. Logarithmic scale on x-axis units in μm.

Aerosols are divided by size into three modes: nuclei mode in which particles range from 0.005 to 0.1 μm in diameter, accumulation mode where particles are 0.1 to 2.5 μm in size and coarse mode which are the particles larger than 2.5 μm (Seinfeld and Pandis, 1998). Figure 2 shows the various types of aerosol formation processes as a function of size. The majority of atmospheric aerosols are found in the nucleation mode and result from primary emission sources in addition to secondary aerosol processes. Larger particles are more readily removed

from the atmosphere by rainout or sedimentation, as indicated by their distribution number in the schematic.

Depending on their size, aerosol particles can have serious effects on health with smaller particles posing a more serious threat because of their ability to become trapped within the respiratory pathways (Seaton, 1995). Various studies have linked fine particles with significant health problems including chronic bronchitis and aggravated asthma, and as a result there are regulations in place which attempt to reduce concentrations of such particles in the air (Seaton, 1995). The Environmental Protection Agency (EPA) has mandates in place which limit the amount of particulate matter smaller than 2.5 μm and 10.0 μm over a 24-hour time period and annually (U.S. EPA, 1996). In the case of $PM_{2.5}$, concentrations must not exceed 35.0 μg m^{-3} within a 24-hour period and the annual average must be less than 15.0 μg m^{-3} (U.S. EPA, 1996). For example, a soot particle with a diameter of 0.3 μm has a density of 0.3 g cm^{-3} and a volume of 1.4×10^{-14} cm^3, and using the annual mean of 15.0 μg m^{-3} equals 2100 soot particles per cm^3 of air. Such high concentrations of soot are not uncommon in urban areas (Zielinski et al. 1997). The lifetime of aerosol in the atmosphere is relatively short, on the order of a few days to a few weeks (Sienfeld and Pandis, 1998). Particles are removed from the atmosphere by two mechanisms: dry deposition or wet deposition in which they are incorporated into cloud droplets during the formation of precipitation (Seinfeld and Pandis, 1998). Aerosol particles that can become activated to grow to cloud droplets or form ice under certain conditions are termed cloud condensation nuclei (CCN) and ice nuclei (IN) respectively.

1.3 Atmospheric Ice Formation

The ability of aerosol to act as CCN or IN is a very importance process in the atmosphere, that depends upon atmospheric conditions in addition to the properties of the aerosol particle (Seinfeld and Pandis, 1998). The surface properties dictate how efficient water vapor is able to condense onto the surface of a specific particle type in addition to whether it will be a good IN (Pruppacher and Klett, 1997). Additionally, the air must be supersaturated with respect to water and the temperature is crucial. Figure 3 shows the likely existence of various phases within clouds as a function of temperature, in which as the temperature decreases, the likelihood of ice being present increases, and at -20°C only 10% of clouds consist entirely of water drops (Seinfield and Pandis, 1998; Boronikov et al., 1963). Instead the clouds that exist are more likely to be mixed phase clouds consisting of liquid and ice particles or exclusively ice particles (Seinfield and Pandis, 1998; Boronikov et al., 1963). Low level mixed phase clouds have been found to be quite prevalent in the Arctic region where they vary significantly in terms of IN concentration, with fewer IN leading to an increase in cloud lifetime (Curry et al., 1996; Jiang et al., 2000). The impact of these mixed phase clouds on climate, however is not entirely understood, partially due to the lack of understanding associated with the microphysical properties of ice nucleation (Vavrus, 2004; Lubin and Vogelmann, 2006).

Aerosol particles acting as ice nuclei can initiate ice nucleation and induce cirrus cloud formation (Pruppacher and Klett, 1997). Cirrus clouds cover roughly 30% of Earths surface and play a key role in the regulating of radiative fluxes (Wylie et al., 2005; Chen et al., 2000). This is due to their proficiency in trapping outgoing terrestrial radiation, resulting in a predominantly warming effect on the atmosphere (Hartmann et al., 1992; Chen et al., 2000). Ice particles can also affect the water vapor budget in the upper troposphere and lower stratosphere (UT/LS) by dehydration due to sedimentation (Holton et al., 1995). This subsequently alters the hydrological cycle and radiative budget along with stratospheric chemical composition (Held and Soden, 2000; Lelieveld et al., 2007; Jensen and Pfister, 2004; Peter et al., 2003). Given the importance of cirrus clouds, the mechanisms namely,

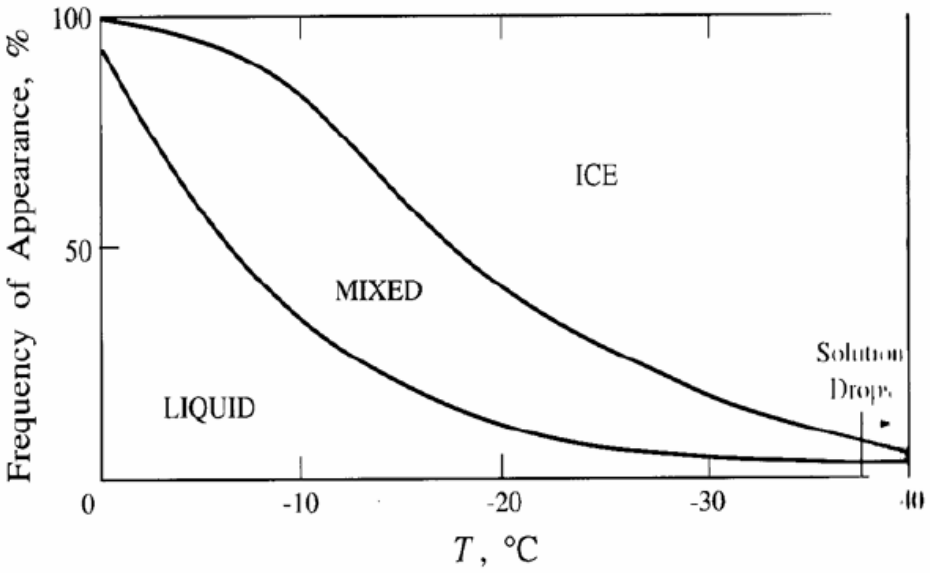

Figure 3: Average frequencies of appearance of supercooled water, mixed phase, and ice clouds as a function of temperature in layer clouds over Russia (Boronikov et al., 1963). At warmer temperatures almost all of water in clouds exists in liquid form, however as temperature decreases, the probability of existence of liquid water also does.

homogeneous and heterogeneous ice nucleation, by which ice clouds form need to be better understood requiring additional studies (Pruppacher and Klett, 1997; Forster et al., 2007).

Homogenous ice nucleation refers to ice formation from a purely liquid and supercooled aqueous solution as opposed to heterogeneous ice nucleation in which ice formation is initiated from a pre-existing substrate, (IN) (Pruppacher and Klett, 1997). The aerosol particle or pre-existing substrate, is referred to as being supercooled or metastable since freezing is kinetically hindered (Pruppacher and Klett, 1997). Homogenous ice nucleation occurs at lower temperatures and higher supersaturations of water vapor than heterogeneous ice nucleation, thus heterogeneous may be a more important pathway at atmospherically relevant conditions (Pruppacher and Klett, 1997).

Heterogeneous ice nucleation can proceed via four pathways, so-called "modes"; condensation (ice nucleates during water vapor condensation onto the IN at temperatures below the ice melting point), immersion (ice nucleates from an IN immersed in a supercooled aqueous droplet), contact (ice formation is induced by collision of supercooled droplets with IN), and

deposition mode (ice nucleates on an IN directly from supersaturated water vapor) (Pruppacher and Klett, 1997; Vali, 1985). In situ measurements have shown that immersion and condensation freezing appear to be the dominant freezing mechanism within ice and mixed-phased clouds (Prenni et al., 2009) Heterogeneous nucleation is governed by the surface properties of the ice nuclei, specifically size and morphology, solubility, and active site distribution, all of which dictate nucleation efficiency (Pruppacher and Klett, 1997). Different methods take different approaches to describe the process of ice nucleation, the most popular being Classical Nucleation Theory.

Classical Nucleation Theory (CNT) relies on kinetic and thermodynamic properties to described homogeneous and heterogenous ice nucleation, in which two energy barriers must be overcome (Pruppacher and Klett, 1997). Heterogeneous nucleation according to CNT involves a fractional reduction, f_{het}, in one of the energy barriers due to the presence of the ice nuclei (Pruppacher and Klett, 1997). Water-activity (a_{w}) based theorem is a modification of CNT originally employed to describe homogeneous ice nucleation (Koop et al., 2000), in which a homogenous nucleation rate coefficient, J_{hom}, is obtained in units of $\mathrm{cm}^{-3}\mathrm{s}^{-1}$. This approach states that the freezing of an aqueous aerosol is independent of the nature of the solute and only depends on the a_{w} of the solution (Koop et al., 2000). Recent studies have shown this method is successful in describing immersion freezing of various ice nuclei (Zobrist et al., 2008; Koop and Zobrist, 2009). Both CNT and the a_{w} theory are time-dependent descriptions, as opposed to the Singular Hypothesis (SH), which is a time-independent approach. In the SH approach, heterogeneous ice nucleation only depends upon temperature, in which the ice nuclei becomes activated once a certain temperature is achieved (Vali, 1971). SH derives the cumulative ice nuclei spectra, K, in units of cm^{-2}. The 3 methods described above will be used and compared to generate ice particle production estimates in the atmosphere with subsequent effects on the global radiative budget (Jensen et al. 2001).

1.4 Radiative Effects of Aerosol and Clouds

The Earth's climate is controlled by the balance between the incoming solar radiation and outgoing terrestrial radiation into space. This balance referred to as the global radiative budget, is heavily influenced by many factors including that of gaseous and aerosol species present in the atmosphere, specifically the troposphere. A measure of how the energy balance of the Earth-atmosphere system is influenced when factors that affect climate are altered, is termed "radiative forcing" (Forster et al., 2007). Radiative forcing is defined by Forster et al., (2007) as 'the change in net (down minus up) irradiance (solar plus longwave; in W m^{-2}) at the tropopause after allowing stratospheric temperatures to readjust to radiative equilibrium, but with surface and tropospheric temperatures and state held fixed at the unperturbed values'.

The influence of aerosol particles on the global radiative budget can be divided into the direct and indirect effects. The direct effect describes the interactions of the aerosol with radiation. The indirect effect encompasses the ability of aerosol particles to act as CCN or IN, altering cloud radiative properties (Twomey, 1974; Albrecht, 1989; Baker, 1997; Rosenfeld, 2000; Ramanathan et al., 2001; Forster et al., 2007; Baker and Peter, 2008). The 2007 report by the Intergovernmental Panel on Climate Change (IPCC) summarized factors contributing to changes in the global radiative forcing and thus climate change, shown in Figure 4. Greenhouse gases, such as carbon dioxide (CO_2) are among the components that have been identified as having a significant positive effect on the global radiative budget and are therefore a major contributor to the warming of the Earths atmosphere (Forster et al., 2007). In contrast it is estimated that biomass burning aerosol can have an overall negative impact on the global radiative budget, i.e. a cooling effect on the earth's atmosphere (Forster et al., 2007). As highlighted in Figure 4 by the error bars, there are large uncertainties associated with both the aerosol direct and indirect effects (Forster et al., 2007), especially the indirect effect.

Aerosol particles in the atmosphere directly interact with incoming solar radiation by

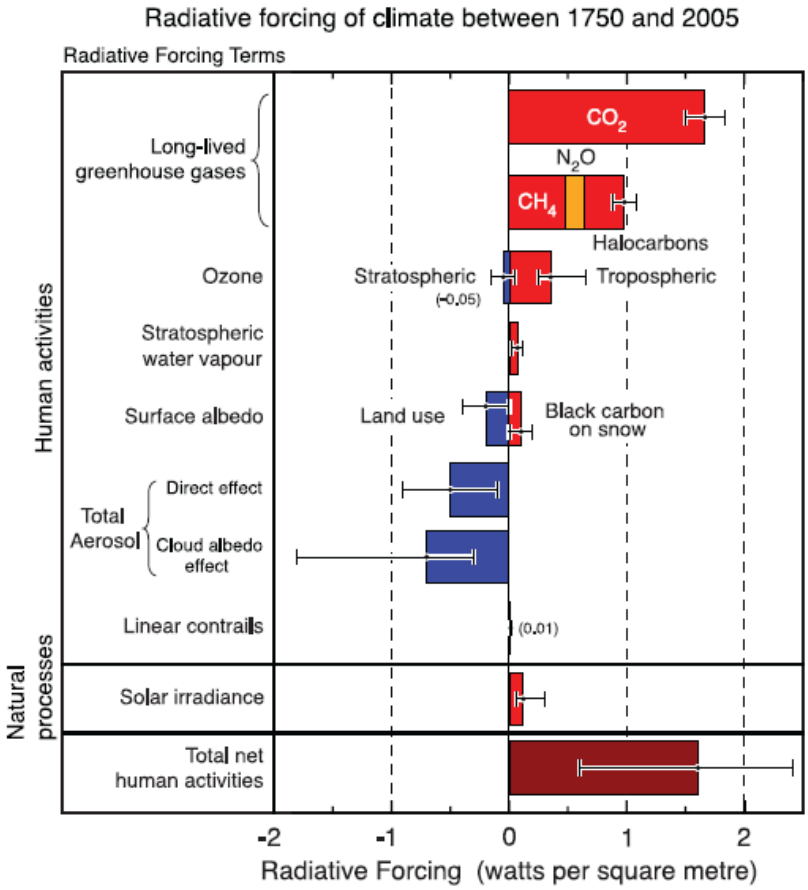

Figure 4: Summary of the radiative forcing of climate change which result from factors associated with natural processes as well as human activities. The values represent the forcings in 2005 relative to the start of the industrial era (about 1750). Human activities cause significant changes in long-lived gases, ozone, water vapor, surface albedo, aerosols and contrails. The only increase in natural forcing of any significance between 1750 and 2005 occurred in solar irradiance. Positive forcings lead to warming of climate and negative forcings lead to a cooling. The thin black line attached to each colored bar represents the range of uncertainty for the respective value. (Figure and caption adapted from IPCC AR4 report.) (Forster et al.2007)

scattering and absorption. The direct effect of aerosol particles depends on size, morphology, composition, and number concentration of the aerosol, all of which influence optical properties (Albrecht, 1989; Forster et al., 2007). The phase and radius of the aerosol particle have significant implications on optical properties as relative humidity and temperature varies throughout the atmosphere both of which alter the size and phase of the aerosol (Seinfeld and Pandis, 1998). A large source of the uncertainty in the direct effects of aerosol is associated with quantifying both primary and secondary emission sources in order to get an accurate

concentration of aerosol in the atmosphere (Forster et al., 2007).

The aerosol indirect effect encompasses their ability to act as cloud condensation nuclei (CCN) and ice nuclei (IN) modifying cloud formation processes and thus their radiative properties (Charlson et al., 1992; Twomey, 1974; Jensen and Toon, 1994). Anthropogenic sources such as biomass burning and fossil fuel combustion increase the number of aerosol particles in the atmosphere, and therefore CCN and IN. The increase in the number of cloud droplets results in a smaller average cloud droplet size, which in turns results in more solar radiation being reflected back towards space (Twomey, 1974). The second indirect effect refers to the suppressed precipitation due to the reduction in cloud droplet size and the increased thickness of clouds due to the increase of cloud droplet number density (Albrecht, 1989; Pincus and Baker, 1994; Forster et al., 2007). The direct and various indirect aerosol effects are summarized in Figure 5. Whereas an increasingly improved understanding of the role of CCN on climate is being achieved (Forster et al., 2007), the effect of IN on the atmosphere is still not well understood (Forster et al., 2007)

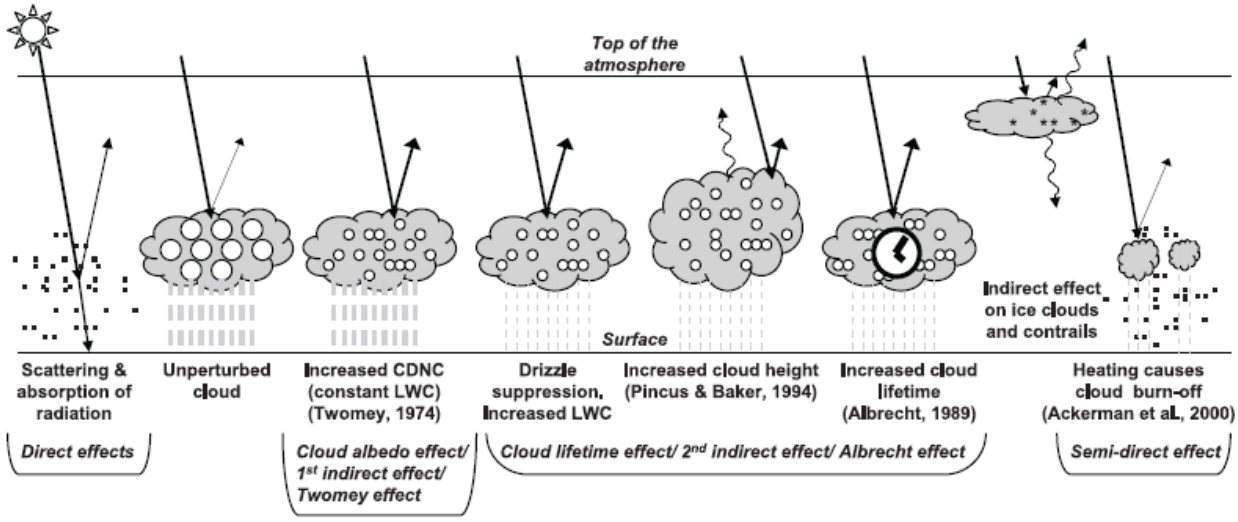

Figure 5: Direct and Indirect Effect of Aerosols. Various radiative mechanisms associated with cloud effects. Black dots represent aerosol particles, open circles are cloud droplets and black stars are ice crystals. Straight lines represent incoming and reflected solar radiation, wavy lines represent terrestrial radiation. The unperturbed cloud contains only natural aerosol and opposed to the other clouds which contain more CCN due to anthropogenic and natural aerosols; increased cloud droplet number concentration (CDNC). Vertical grey lines represent rainfall, and LWC is the liquid water content. (Figure and caption adapted from IPCC AR4 report.) (Forster et al.2007)

Cirrus clouds are present in the upper troposphere, where temperatures are low enough to facilitate their formation. The radiative properties of cirrus clouds depend upon the crystal shape, number concentration, and optical depth of the cloud (Chen et al., 2000). Previous modeling studies have found that ice clouds exhibit a positive radiative forcing on the climate due to their proficiency in trapping outgoing radiation (Chen et al., 2000). The radiative forcing of ice clouds are not included in the IPCC Fourth Assesment Report due to many uncertainties associated with ice cloud nucleation and microphysical mechanisms (Forster et al., 2007). One way to improve the understanding of ice nucleation is to preform laboratory experiments and compare results with proposed mechanisms. Previous studies have shown the local and long-range transport of anthropogenic aerosols can influence IN concentrations within ice and mixed phased clouds (Prenni et al., 2009). This has serious implications on the radiative properties of such clouds as they are heavily dependent upon IN concentration (Curry et al., 1996). In situ measurements have shown that IN with a high carbonaceous fraction, resulting from biomass burning origin have been observed in mixed phase clouds (Prenni et al., 2009).

1.5 Biomass Burning Aerosol

Biomass burning consumes a significant amount of vegetation every year, estimates that 3.5 million km^2 of land burned in 2000 (Tansey et al., 2004), roughly a third of the size of the United States of America. Although biomass burning is often a natural occurrence due to lighting strikes and volcanic activity, many biomass events can be linked to anthropogenic sources (Myers, 1991; Crutzen and Andreae, 1990). With the occurrence of each event, the spectrum of chemicals emitted into the atmosphere is vast in terms of phase, size, and composition (Andreae and Merlet, 2001). A substantial amount of carbon emitted from

biomass burning includes the following gaseous species: CO_2, CO and CH_4. CO_2 and CH_4 which have been identified as major contributors to global warming due to their interaction with solar and terrestrial radiation, their relative concentrations and their long lifetime of 10 and 9 years, respectively (Wallace and Hobbs, 2006). Biomass burning is a major source of atmospheric aerosol, emitting an estimated 39% of the total global particulate organic carbon load (Andreae, 1991).

Biomass burning aerosol (BBA) particles consist of a complex mixture of inorganic and water-soluble and water-insoluble organic compounds exhibiting different morphologies and phases (Andreae et al., 1998; Posfai et al.,1998; Posfai et al., 1999; Buseck and Posfai,1999; Schauer et al., 2001; Hays et al., 2002; Li et al., 2003; Posfai et al., 2003; Hudson et al., 2004; Iinuma et al., 2007; Li et al., 2010) For example, BBA particles have been associated with soot (elemental carbon), tar balls, potassium-salt particles, mineral dust, ammonium sulfate, and organics and respective mixtures of these individual compounds (Li et al., 2003; Posfai et al., 2003; Schauer et al., 2001; Iinuma et al., 2007; Li et al., 2010). Table 1 summarizes major compounds representative of water-soluble and water-insoluble organic carbon (not accounting for elemental carbon) and inorganic ions identified in various biofuel sources such as grasses and trees indicating the range of particle compositions observed (Schauer et al., 2001; Iinuma et al., 2007). As a major organic species of BBA particles, levoglucosan (1,6-anhydro-β-D-glucopyranose, $C_6H_{10}O_5$) has been identified followed by other cellulose and hemicellulose decomposition products (Schauer et al., 2001; Simoneit, 2002; Iinuma et al., 2007). Laboratory studies indicate that a significant amount of ammonium and sulfate are often associated with the organic mass fraction (Schauer et al., 2001; Iinuma et al., 2007). This is also corroborated by field measurements indicating that BBA particles can contain ammonium (Andreae et al., 1998; Posfai et al.,1998; Posfai et al., 1999; Buseck and Posfai,1999; Hays et al., 2002; Li et al., 2003; Posfai et al., 2003; Hudson et al., 2004; Li et al., 2010). In the atmosphere, tropospheric particles often resemble internal mixtures of sulfates and carbonaceous material (Murphy et al., 1998; Murphy et al., 2007; Froyd et al.,

2009).

Table 1: Major compounds identified in biomass burning aerosols are given. The numbers are compiled from a study of Schauer et al., 2001 and Iinuma et al., 2007. The organic compound class and mass fraction and representative organic species are given.

organic compounds	mass fraction in wt%	mass fraction in wt%	representative organic species
substituted phenols	6	1	benzenediol, hydroxybenzoic acid
substituted guaiacols	7	1	guaiacylacetone, vanillic acid
substituted syringols	8	1	methylsyringol, syringic acid
resin acids	4	2	pimaric acid, abietic acid
anhydro-sugars	30	60	levoglucosan
sugars	5	12	glucose, galactosan, mannosan
alkenoic acids	1		octadecenoic acid
other organic compounds (alkanes, alkanoic acids)	4	3	hexadecanoic acid, docosanoic acid docosane, nonacosane, hentriacontane
inorganics	0.5–20	11	Cl^-, NO_3^-, SO_4^{2-}, Na^+, NH_4^+, K^+, Mg^{2+}, Ca^{2+}

Another class of organic material which has been identified in ambient aerosol particles originating from biomass burning are humic acid like substances (HULIS) (Mukai and Ambe, 1986; Facchini et al., 1999; Zappoli et al., 1999; Graham et al., 2002; Mayol-Bracero et al., 2002; Graber and Rudich, 2006). HULIS are high molecular weight conglomerates which contain a mixture of water soluble and water insoluble compounds (Graber and Rudich, 2006). Previous studies have shown a strong interaction of ammonium with HULIS, and thus the two can exist within the same system (Stevenson, 1982). In addition to biomass burning, other sources of HULIS include fossil fuel combustion, secondary organic aerosol formation, and marine sources (Simoneit, 1980; Cini et al., 1994; Cini et al., 1996; Calace et al., 2001; Cavalli et al., 2004; Gelencser et al., 2002; Jang et al., 2002; Jang et al., 2003; Tolocka et al., 2004; Hung et al., 2005).

Biomass burning plumes can extend deep into the upper troposphere/ lower stratosphere where temperatures are low enough for ice formation to occur (Fromm et al 2000, 2005; Wotawa and Trainer, 2000). Previous studies also have shown that polar mixed phase clouds have been impacted by carbonaceous particles from biomass burning (Prenni et al., 2009).

Ice crystal observations indicate that IN residues for cirrus and mixed phase clouds contain some organic material in some instances (Froyd et al., 2010). Leonardite and Pahokee Peat are commercially available humic acids, which have been previously used as surrogates of atmospheric HULIS for studies involving their ability to act as IN (Kanji et al. 2008; Wang and Knopf, 2011; Fornea et al., 2009). These studies have investigated these two substrates in the deposition mode but not in the immersion mode although immersion mode has been observed to be a predominant pathway for heterogeneous ice nucleation (Prenni et al., 2009).

1.6 Objectives of this thesis

This thesis describes research which explored the ice forming potential of particles serving as surrogates of biomass burning aerosols. Homogeneous ice nucleation studied explored inorganic/ organic mixtures of $(NH_4)_2SO_4$/ levoglucosan of mass ratios: 10:1, 1:1, 1:5, and 1:10. Two additional systems consisting of multi-component water soluble organic compounds with and without $(NH_4)_2SO_4$ were also explored. Freezing temperatures and melting temperatures were obtained and subsequent homogeneous ice nucleation rate coefficients derived for 6 different aqueous droplet compositions as a function of relative humidity, and temperature. The results are then compared to the water-activity based theory. These aqueous droplets represent idealized particle compositions compared to field-collected and laboratory-generated BBA particles (Andreae et al., 1998; Posfai et al.,1998; Posfai et al., 1999; Buseck and Posfai,1999; Schauer et al., 2001; Hays et al., 2002; Li et al., 2003; Posfai et al., 2003; Hudson et al., 2004; Iinuma et al., 2007; Li et al., 2010). They serve as surrogates for the water-soluble organic fraction of BBA particles and typical organic containing tropospheric aerosol particles to investigate the potential to initiate ice formation via homogeneous nucleation.

The heterogeneous ice nucleation study investigated the ice nucleating ability of Pahokee

Peat and Leonardite, two surrogates of HULIS, immersed in aqueous $(NH_4)_2SO_4$. Freezing temperatures and melting temperatures were obtained and subsequent heterogenous ice nucleation rate coefficients derived for the 2 IN as a function of relative humidity, and temperature. The results have then been analyzed in the framework of classical nucleation theory, water-activity based theory, and singular hypothesis. Ice particle production was acquired for the investigated systems under atmospherically relevant conditions.

2 Theory

2.1 Water Vapor and RH

Water in the atmosphere exists in the gas phase as water vapor and in the liquid phase as water droplets and wet aerosol particles (Seinfeld and Pandis, 1998). Thermodynamic principles are needed to describe the processes involving the interactions between water vapor and aqueous phase systems. These principles are examined in the context of atmospheric conditions in which temperature, pressure and solution composition are varying. The Gibbs free energy, G, of a system is defined as

$$G = U + pV - TS \ , \tag{1}$$

where U is the internal energy of the system, p and V is its pressure and volume, S is the entropy of the system, and T is absolute temperature. The behavior of species i in a solution can be described by its chemical potential μ_i, shown below

$$\mu_i = \left(\frac{\partial G}{\partial n_i}\right)_{T,p,n_j} \ , \tag{2}$$

where T, p, and moles of additional other solution species, n_j, are held constant. The total Gibbs free energy of the system is the sum of all the single chemical potentials weighted by the corresponding number of moles.

The chemical potential of an ideal solution of mole fraction, x_i, is defined by

$$\mu_i = \mu_i^*(T,p) + RT\ln x_i \tag{3}$$

where μ_i^* is the chemical potential of the pure species (x_i) under the same pressure and temperature, and R is the universal gas constant. However atmospheric aerosols are not ideal solutions and can deviate significantly. The deviation from ideality is described by

introducing the activity coefficient, γ_i, therefore the chemical potential is given by

$$\mu_i = \mu_i^*(T, p) + RT\ln(\gamma_i x_i) \tag{4}$$

where the activity coeffient is a function of p, T, and x_i (Seinfeld and Pandis, 1998). For an ideal solution $\gamma_i = 1$. The product of the mole fraction, x_i, of a solution component and its activity coefficient γ_i is defined as the activity, a_i and is shown below.

$$a_i = \gamma_i x_i \tag{5}$$

Aqueous particles are of particular importance for this study, in which water activity, a_{w}, is derived as the following

$$a_{\mathrm{w}}(T) = \frac{p_{\mathrm{H_2O}}(T)}{p^{\circ}_{\mathrm{H_2O}}(T)} = \frac{RH}{100} \tag{6}$$

where $p_{\mathrm{H_2O}}$ is the water vapor pressure of the solution and $p^{\circ}_{\mathrm{H_2O}}$ is the water vapor pressure of pure water at the same temperature. It is also important to note that when in equilibrium, a_{w} is equal to relative humidity, RH. Aerosol particles experience phase transitions due to changes in atmospheric conditions, i.e. temperature and RH variations. The transition from ice to liquid is significantly different from the transition of liquid to ice. Figure 6 illustrates the two fundamental differences between the two phase transitions. Thermodynamically, the warming of a frozen liquid adds some amount of heat to the system. This energy added excites molecules within the solid causing bonds to break, and if a sufficient amount of energy is added, the solution will transition solid to liquid. The phase transition from solid to liquid is an equilibrium process

Both homogeneous nucleation and heterogeneous nucleation occur in supersaturated en-

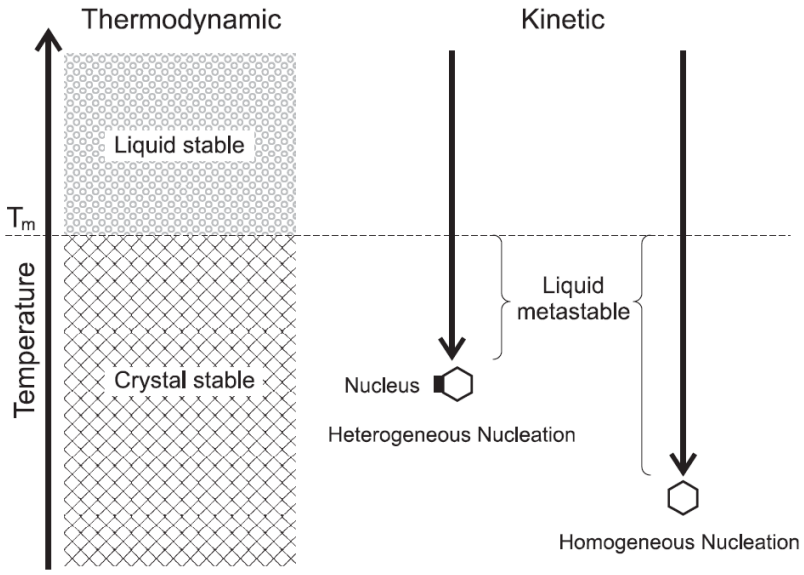

Figure 6: Schematic picture comparing different nucleation mechanisms for the freezing of a liquid. T_{m} is the melting point of the crystalline phase.

vironments. S, the saturation ratio, is defined as

$$S(T) = \frac{p^l_{\mathrm{H_2O}}(T)}{p^s_{\mathrm{H_2O}}(T)} \,, \tag{7}$$

where $p^l_{\mathrm{H_2O}}$ and $p^s_{\mathrm{H_2O}}$ are the vapor pressures of pure liquid water and ice respectively at the same conditions. When a liquid is saturated with respect to its solid then $S = 1$. Homogenous or heterogenous nucleation will not occur unless $S > 1$ (Pruppacher and Klett, 1997; Seinfeld and Pandis, 1998). As the temperature decreases, S increases, facilitating favorable nucleation conditions.

There have been a variety of approaches introduced which attempt to describe the process of ice nucleation (Pruppacher and Klett, 1997). The most widely used is Classical Nucleation Theory (CNT), which represents nucleation as a stochastic process, and gives ice nucleation events per unit of time and volume (Pruppacher and Klett, 1997). Another method is the water activity based method, which relies on thermodynamic properties expressed by a_{w}, to describe ice nucleation (Koop et al., 2000). The last approach discussed in this thesis is singular hypothesis, which is a time independent approach, which yields cumulative freezing

spectra (Vali, 1971).

2.2 Homogeneous Ice Nucleation

2.2.1 Classical Nucleation Theory

According to classical nucleation theory (CNT), homogeneous nucleation is initiated by the aggregation of water molecules into clusters (Pruppacher and Klett, 1997). A specific number of molecules must be present to form a critical cluster, at which point nucleation will likely occur (Seinfeld and Pandis, 1998). Homogeneous nucleation depends on the transfer of molecules from the liquid to the solid phase, i.e. the formation of the critical cluster. The formation of the critical cluster is heavily dependent upon S, in which if S is large enough, the critical cluster size will be exceeded and the growth of a new phase is initiated (Seinfeld and Pandis, 1998). The transfer of i molecules from the liquid phase forms an i-mer cluster of radius r. The change in the Gibbs free energy is

$$\Delta G_i = (\mu_{sol} - \mu_{liq})i + 4\pi\sigma_{sol}r^2 \tag{8}$$

where μ_{sol} and μ_{liq} are the chemical potentials of the solid and liquid phase, respectively. σ_{sol} is the surface tension between the solid and liquid phase and r is radius of the critical cluster. The number of molecules in the solid, i, can be obtained by

$$i = \frac{V_{sol}}{v_{sol}} = \frac{4\pi r^3}{3v_{sol}} \tag{9}$$

where V_{sol} is the volume of the critical cluster and v_{sol} is the volume of one i-mer in the solid. The difference in chemical potentials can also be expressed in terms of partial pressures or

the saturation ratio, S as

$$\mu_{liq} - \mu_{sol} = kT\ln\frac{p_{\mathrm{A}}^{l}}{p_{\mathrm{A}}^{s}} = kT\ln S \tag{10}$$

where k is the Boltzmann constant. Combining the equations (8), (9), and (10), we arrive at the following expression

$$\Delta G_i = 4\pi\sigma_{sol}r^2 - \frac{4\pi}{3}\frac{kT\ln S}{v_{sol}}r^3 \tag{11}$$

for the Gibbs free energy change of i-mer formation. The first term is the free energy increase as a result of the formation of a surface area at the critical cluster. The second term is the free energy decrease due to the transfer of molecules from the liquid to the solid phase. Here it is assumed that the critical cluster has the same properties as the bulk. Furthermore, surface tension, σ_{sol}, is not known for a small critical radius at low temperatures. It is known for a few pure substances at the melting temperature of the bulk crystal, and thus assumed to be an appropriate description. These assumptions are the source of much disagreement involving CNT.

The gibbs free energy change due to the formation of a critical cluster is heavily dependent upon S, in addition to the size of the critical cluster, r^*, as depicted in Figure 6. The critical i-mer radius is derived by

$$r^* = \frac{2\sigma_{sol}v_{sol}}{kT\ln S} \tag{12}$$

The Gibbs free energy at $r*$ is then obtained by combining equations (11) and (12), resulting in

$$\Delta G^* = \frac{16\pi v_l^2\sigma_{sol}^3}{3(kT\ln S)^2}\ . \tag{13}$$

An increase in S will in turn decrease the Gibbs free energy barrier ΔG^*. Also depicted

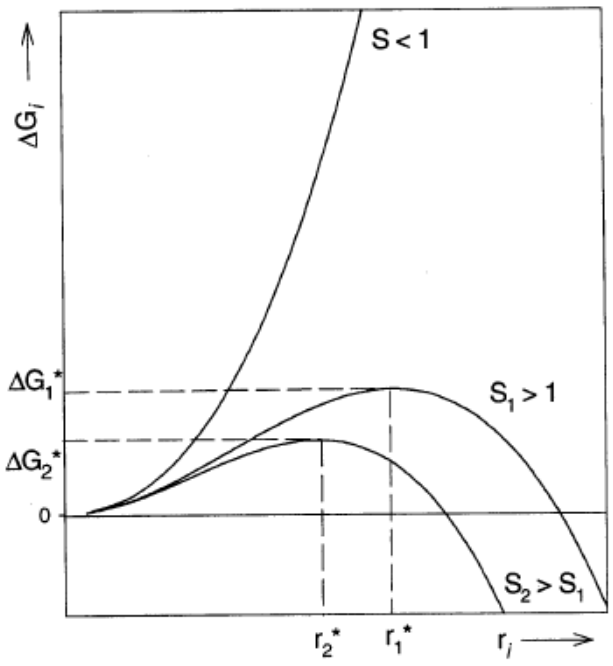

Figure 7: The Gibbs free energy difference due to the formation of a critical cluster as a function of saturation ratio S and critical cluster size, r^*.

in the figure is the strong dependence on r^*. If the size of the cluster is smaller than that of the critical cluster, r^*, the molecules will dissociate to a more energetically favorable state. If the cluster reaches the critical radius,r^*, nucleation will start due to the decrease in ΔG, however an additional energy barrier must be overcome, which describes the energy needed for the diffusion of molecules to the cluster, ΔF. Combining the two energy barriers the homogeneous nucleation rate coefficient, J_{hom}, in units of $\text{cm}^{-3}\text{s}^{-1}$ can then be expressed as:

$$J_{\text{hom}}(T) = \frac{kT}{h}\exp\left[-\frac{\Delta F(T)}{kT}\right] \times n\exp\left[-\frac{\Delta G(T)}{kT}\right] , \tag{14}$$

where h is Planck constant, and n is the number of density of water molecules (Pruppacher and Klett, 1997; Seinfeld and Pandis, 1998). In the equation above J_{hom} is the number of nucleation events per volume of liquid and time.

CNT has been shown to be very successful in various disciplines, but its disadvantage arises from the fact that it relies on macroscopic properties for the description of micro-

scopic properties of the ice cluster (Pruppacher and Klett, 1997; Seinfeld and Pandis, 1998). Furthermore, σ_{sol} and ΔF are only available for a few aqueous solutions, but not in the supercooled region. A theory termed the water activity based ice nucleation sought to describe nucleation without knowledge of the microscopic properties (Koop et al., 2000).

2.2.2 Water Activity Based Theory

In 2000, Koop et al. proposed a new mechanism for predicting homogenous freezing temperatures and homogeneous nucleation rate coefficients, this was termed the water-activity-based ice nucleation theory and will be abbreviated KO00. KO00 states that homogeneous nucleation of ice from supercooled aqueous solutions is independent of the nature of the solute and only depends on the water activity, a_{w}, of the solution (Koop et al. 2000). In this approach thermodynamic principles are applied to the kinetic process of ice nucleation.

According to KO00, the homogenous freezing curve can be derived by shifting the melting curve by Δa_{w}, this is shown by equation 15 (Koop 2000).

$$a_{\mathrm{w}}^{\mathrm{f,hom}}(T) = a_{\mathrm{w}}^{\mathrm{ice}}(T) + \Delta a_{\mathrm{w}} \tag{15}$$

The melting curve is parameterized by the following equation by Koop et al. (2000)

$$a_{\mathrm{w}}^{\mathrm{ice}}(T) = exp[(210368 + 131.438T - 3.32373 \times 10^6 T^{-1} - 41729.1 lnT)/RT] \tag{16}$$

where R is the ideal gas constant. Show in Figure 8 is the melting line described above as a function water activity and temperature and the resulting shift which yields homogeneous freezing line and heterogeneous freezing as well. The freezing line also corresponds to a J_{hom} value, as predicted by KO00 (Koop et al., 2000)

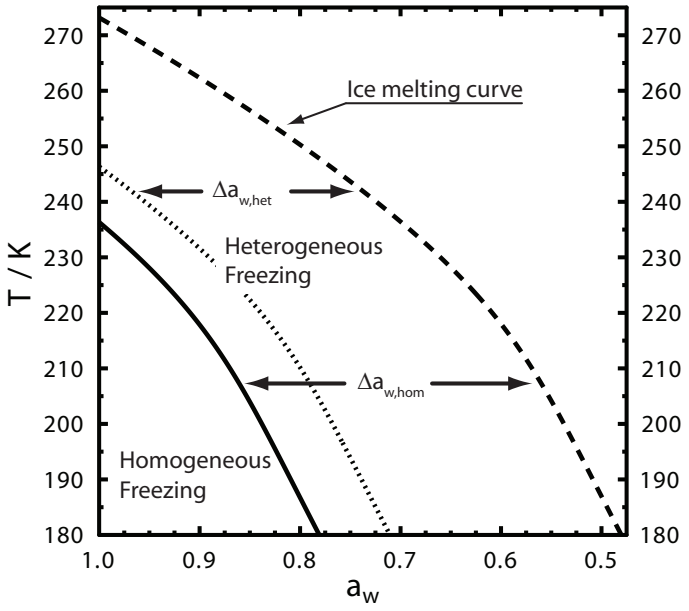

Figure 8: An illustration of the water activity approach adopted from Koop et al., (2000) and Koop and Zobrist (2009) to describe homogeneous and heterogeneous freezing temperatures of micrometer sized aqueous solution droplets. The homogeneous and heterogeneous freezing curves are depicted as solid and dotted lines. The ice melting curve is indicated. Pure water corresponds to $a_{\mathrm{w}} = 1.0$, and $a_{\mathrm{w}} < 1.0$ corresponds to more concentrated solutions.

One of the major shortfalls of the water-activity based theorem is that it requires that a_{w} is known at low temperatures, which has been problematic, due to the lack of experimental data at lower temperatures. In the absence of such data, Koop et al., (2000) suggested that a_{w} at freezing temperatures may be obtained from the a_{w} at the melting point of the aqueous solution. This approach assumes a_{w} does not change with T, however other studies have shown that a_{w} can deviate significantly with decreasing temperatures, especially in the case of aqueous organic solutions (Koop, 2004; Zobrist et al., 2003; Zobrist et al., 2008; Knopf and Lopez, 2010;). Aqueous levoglucosan particles deviate significantly from their a_{w} at the melting point as temperatures decrease (Knopf and Lopez, 2010), however no studies have examined the effect of an inorganic species such $(NH_4)_2SO_4$ as combined with levoglucosan in the bulk phase until now (Knopf and Rigg, 2011). The water-activity based theorem will be employed in this study in analyzing the homogeneous freezing and melting temperature of aqueous $(NH_4)_2SO_4$/levoglucosan particles (Knopf and Rigg, 2011).

2.3 Heterogeneous Ice Nucleation

2.3.1 Classical Nucleation Theory

Homogeneous nucleation rates are directly proportional to the volume of the droplet, contrary to heterogeneous nucleation rates which are proportional to the surface area of the ice nuclei (Pruppacher and Klett, 1997). J_{het} is defined as the number of nucleation events per area of the ice nucleus and time ($\text{cm}^{-2}\text{s}^{-1}$).

$$J_{het}(T) = \frac{kT}{h}\exp\left[-\frac{\Delta F(T)}{kT}\right] \times n\exp\left[-\frac{\Delta G(T) f_{\text{het}}(T)}{kT}\right] \tag{17}$$

where k is the Boltzmann constant, h is Planck constant, and n is the number of density of water molecules (Pruppacher and Klett, 1997; Seinfeld and Pandis, 1998). Heterogeneous nucleation is derived from that of homogeneous nucleation with the addition of term, f_{het}, which describes the reduction of Gibbs energy barrier due to the presence of an ice nucleus. This reduction in energy from the term f_{het} is defined as

$$f_{het} = \frac{1}{4}(2 + \cos\alpha)(1 - \cos\alpha)^2 \ . \tag{18}$$

Where α is the concept contact angle in which values range from 0 to 180 (Seinfeld and Pandis, 1998; Pruppacher and Klett 1997). When α is 180, f_{het} becomes 1, and the ice nuclei has no effect on the Gibbs free energy and is thus equivalent to the case of homogeneous nucleation. When α is 0, f_{het} becomes 0 at which point the energy barrier is zero and thus diffusion is the limiting factor, implying a perfect compatibility between the ice nucleus and the ice (Zobrist et al., 2007). Contact angles will be calculated for the two substrates Pahokee peat and Leonardite as a function of temperature.

Classical nucleation theory has been shown to be very successful in various disciplines, but its disadvantage arises from the fact that it relies on macroscopic properties for the description of microscopic properties of the ice embryo (Pruppacher and Klett, 1997). Furthermore, σ, and the diffusion coefficient, D, must be known for the aqueous solution. Although these

values may be available for some aqueous solutions at room temperature, there is almost no data available when it comes to the supercooled region.

2.3.2 Water Activity Based Theory

Similarly to the approach of homogeneous ice nucleation, the heterogeneous freezing curve can be derived by shifting the melting curve by a different Δa_{w}, as depicted in Figure 8 and the Equation 19 (Koop 2000).

$$a_{\mathrm{w}}^{\mathrm{f,het}}(T) = a_{\mathrm{w}}^{\mathrm{ice}}(T) + \Delta a_{\mathrm{w}}^{\mathrm{het}} \tag{19}$$

In addition this theorem will be employed in attempt to describe the heterogeneous freezing and melting involving Pahokee Peat and Leonardite in aqueous $(NH_4)_2SO_4$ particles. Also used to analyze the results from the heterogeneous nucleation study is the singular hypothesis method.

2.3.3 Singular Hypothesis

According to this hypothesis, heterogeneous nucleation is only dependent upon temperature and not time (Vali, 1971). At a single temperature, referred to as the characteristic temperature, T_c, only a specific number of ice nuclei will nucleate ice (Vali, 1971). This process is driven by surface inhomogeneities which act as preferred sites for ice formation, and become activated at T_c (Vali 1971, Vali 1994). The differential ice nuclei spectra, k, quantifies the time independent approach in $\mathrm{cm}^{-2}\mathrm{K}^{-1}$ and is shown by the equation

$$k(T^i) = \frac{1}{A^i_{\rm tot}} \frac{n^i_{\rm nuc}}{\Delta T} \ , \tag{20}$$

where $\mathrm{A}^i_{\rm tot}$ is the total surface area in the droplets that remained liquid at the start of the $i^{\rm th}$ temperature interval (Vali, 1971). A cumulative ice nuclei spectrum as a function of temperature, $K(T^i)$ is derived form experimental data by integrating the differential ice nuclei spectra from the melting temperature to T^i yielding

$$K(T^i) = \sum_{T^{\rm dia}_{\rm m}}^{T_i} \frac{n^i_{\rm nuc}}{A^i_{\rm tot}} \ , \tag{21}$$

where $K(T^i)$ includes the sites which had become ice active for temperatures warmer than T^i. The cumulative ice nuclei spectrum is given in units of cm^{-2}. Derivations of k and K employ $\Delta T = 0.2$ K.

2.4 Diffusion Energy Barrier

The diffusion of water molecules within the aqueous phase has been shown to be an important parameter in CNT. The energy barrier which describes the movement of liquid molecules through solution to the liquid/ice boundary. This can be expressed as follows (Pruppacher and Klett, 1997; Atkins, 1990),

$$\Delta F(T) = \frac{\partial \ln D(T)}{\partial T} kT^2 \ , \tag{22}$$

where D is the diffusion coefficient of water, which can be expressed by the emperical Vogel-Fulcher-Tamman equation as (Smith and Kay, 1999)

$$D(T) = D_0 \exp\left[-\frac{E}{T - T_0}\right] , \tag{23}$$

where D_0, E, and T_0 are fit parameters. Combining Equations 22 and 23, we arrive at the following equation which will be implemented into the results:

$$\Delta F(T) = \frac{kT^2 E}{(T - T_0)}^2 . \tag{24}$$

This equation is valid up to 150 K which is sufficient for this study.

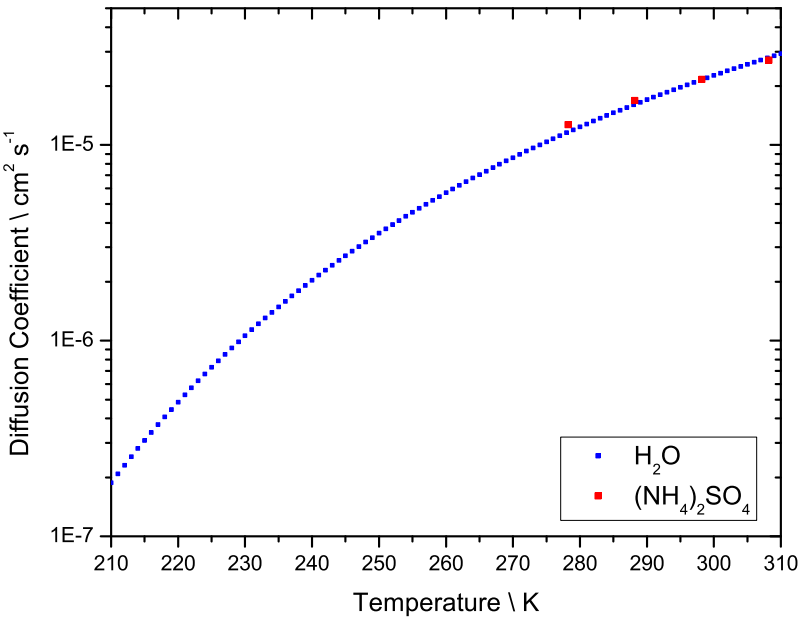

Figure 9: Diffusion coefficient of pure water and subsequent diffusion coefficient of water in $(NH_4)_2SO_4$. (Tanaka, 1974; Smith and Kay, 1999)

For aqueous $(NH_4)_2SO_4$ $D(T)$ is derived from a study by Tanaka (1974) in which the $D_{H_2O}^{(NH_4)_2SO_4}$ is experimentally acquired for a higher wt% solution at temperatures 308 K, 298 K, 288 K and 278 K as shown by red squares. The diffusion coefficients of pure water and

that of water in aqueous $(NH_4)_2SO_4$ as a function of T are very close. We assume that this T dependence is also true for lower wt% solutions in which the two systems are similar enough to where the parameterization by Smith and Kay for pure water can be applied to describe $D_{H_2O}^{(NH_4)_2SO_4}$. Potential uncertainties arising using pure water are minimized as ΔF_{diff} is proportional to the derivative with respect to temperature of the natural logarithm of $D_{H_2O}^{(NH_4)_2SO_4}$ (Zobrist et al. 2007; Knopf and Forrester, 2011). Uncertainties are expected to have a small effect on J_{het} since the derivative is not expected to change significantly (Knopf and Forrester, 2011).

3 Experimental

3.1 Preparation of Aqueous Solutions

For the homogeneous ice nucleation experiments a total of six aqueous solutions were examined. Four solutions with $(NH_4)_2SO_4$/levoglucosan mass ratios of 10:1, 1:1, 1:5 and 1:10, respectively, expressed in corresponding mole ratios of levoglucosan as 0.075, 0.450, 0.803 and 0.891. This is given by the equation

$$x_{\text{lev}} = \frac{n_{\text{lev}}}{n_{\text{lev}} + n_{(NH_4)_2SO_4}} \tag{25}$$

In addition, two aqueous multi-component organic and inorganic/organic solutions shown as mix 1 and mix 2, respectively given in Table 2 were also studied. The appropriate amount of chemicals were weighted, water was added and each solution was placed in the ultrasound bath for 30 minutes to ensure that all reagents were completely dissolved.

Table 2: Composition of aqueous multicomponent organic and inorganic/organic droplets employed in ice nucleation experiments.

organic species	mix 1 (wt%)	mix 2 (wt%)
syringic acid	1.42	1.50
vanillic acid	0.58	0.59
4-hydroxybenzoic acid	0.88	0.93
D-(+)-Mannose	10.97	10.47
D-(+)-Galactose	8.84	8.40
levoglucosan	77.31	73.60
$(NH_4)_2SO_4$	0	4.51

Pahokee peat and Leonardite solutions were prepared in concentrations as shown in Table 3. The Pahokee Peat and Leonardite were first crushed using a mortar and pestle, water added, and the mix placed in an ultrasound bath for 30 minutes, and periodically agitated roughly every 10 minutes. Once the ultrasound bath was complete, the solution was then filtered through a 5 μm filter at which point only particles smaller than 5 μm remained in solution. Additional water passed through the filter into solution with the total water content

quantified in Table 3. Finally, $(NH_4)_2SO_4$ was added to the solution and it was ultimately placed in an ultrasound bath for an hour.

Table 3: Composition of aqueous multicomponent organic and inorganic/organic droplets employed in ice nucleation experiments.

Component	PP/$(NH_4)_2SO_4$ (wt%)	Leo/$(NH_4)_2SO_4$ (wt%)
Pahokee peat	0.02	–
Leonardite	–	0.02
H_2O	93.95	93.95
$(NH_4)_2SO_4$	6.03	6.03

The Pahokee peat appeared to be partially soluble as the solution took on an orange hue within minutes of being placed in the ultrasound bath. Leonardite on the other hand was very insoluble and the fine particles formed a layer on top of the water. Although the Leonardite particles were crushed using the mortar and pestle, when placed in water, a significant amount aggregated to form a large mass, which remained behind after filtering. Although there was little evidence of Leonardite being present in the solution as it maintained a mostly clear appearance, but optical microscopy with 100x magnification, confirmed very fine Leonardite particles were clearly present.

3.2 Particle generation

The appropriate solution was then transferred to a single droplet dispenser apparatus shown in Figure 10. This device consists of a piezo-electric crystalline actuator, which allows droplets to be created on demand through an electrical impulse. Anywhere from 30-60 droplets with diameters ranging from 20-80 μm of identical composition are generated on a glass slide that was previously treated with dimethyldichlorosilane in heptane to provide a hydrophobic coating. The hydrophobic coating is used to reduce the probability of ice nucleation occurring directly on the glass surface (Knopf and Lopez, 2009). This glass slide serves as the bottom of an aerosol cell, which also contained a tin foil spacer coated with high vacuum grease. Sealing of the droplets ensured their exposure to the appropriate RH. All sample preparation steps were done in a clean bench (laminar flow hood) to reduce the

possibility of contamination from random airborne particles.

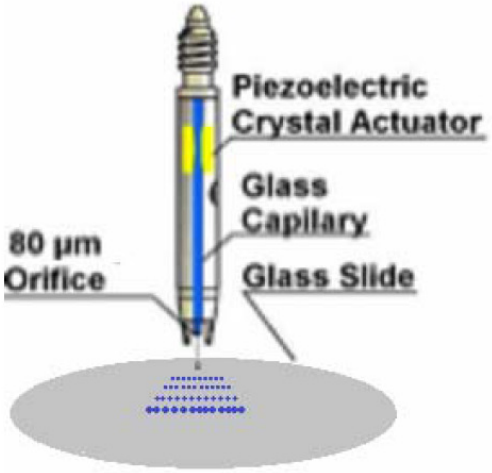

Figure 10: Single drop dispenser shown above (MicroFab Technologies)

3.3 Conditioning of Droplets to Water-Activity

The prepared solution droplets were placed on a custom-made temperature controlled stage within a special conditioning cell (ACC), consisting of a customized glass enclosure with a hydrophobic coating that is designed to expose the droplets to a controlled relative humidity. Figure 6 is a schematic drawing of the various components of the ACC. A controlled flow of N_2(g) passes through a hydrocarbon gas trap followed by a cold trap into a denuder with H_2O submersed in a temperature controlled bath. The temperature of the humidified gas flow, T_{dew}, is quantified by a chilled mirror hygrometer (GE Sensing) before it is introduced into the ACC. Using T_{dew} coupled with the temperature of the stage, T_{stage}, the relative humidity (RH) or a_{w} of the droplets can be calculated using Equation 6. Once the desired conditions are achieved, the droplets are allowed to come into equilibrium, by ensuring that this size remains constant, at which point they are sealed from ambient conditions using a hydrophobic coated glass cover slide. This approach fixes the droplet composition a_{w} at the specific preparation conditions.

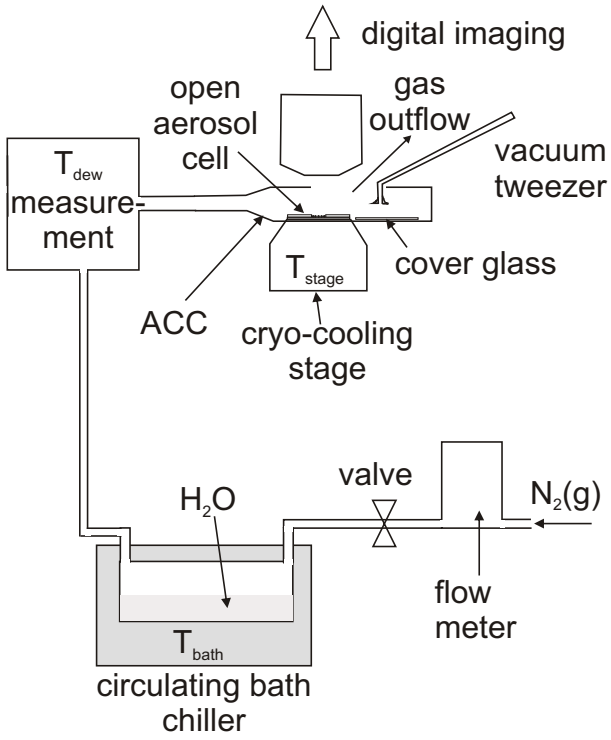

Figure 11: A sketch of the particle exposure setup is shown. The aerosol conditioning cell (ACC) is placed on a home-made cryo-cooling stage which is attached to a home-made reflected light microscope. A gas flow system provides a humidified N_2(g) flow to the ACC. (Figure adapted from Knopf and Lopez, 2009)

3.4 Nucleation Apparatus

The ice nucleation apparatus consists of a temperature controlled stage (Linkam BCS196) that cools the droplets to a pre-selected temperature at a rate of 10 K min^{-1}. A digital camera attached to a microscope enables the droplets to be viewed and photographed at intervals of 0.2 K. After the droplets are frozen, they are warmed up at a specified rate and the melting point is observed and recorded. Once the experiment is completed, analysis begins with the collection of freezing temperatures, melting temperatures and droplet diameters for each individual droplet using imaging software (Northern Eclipse).

3.5 Calibration

The ACC was calibrated with respect to RH by first measuring the melting point $T_{\rm ice}^{\rm melt}$ of ice particles, using 3 independent samples. The frozen droplets were heated at a rate of

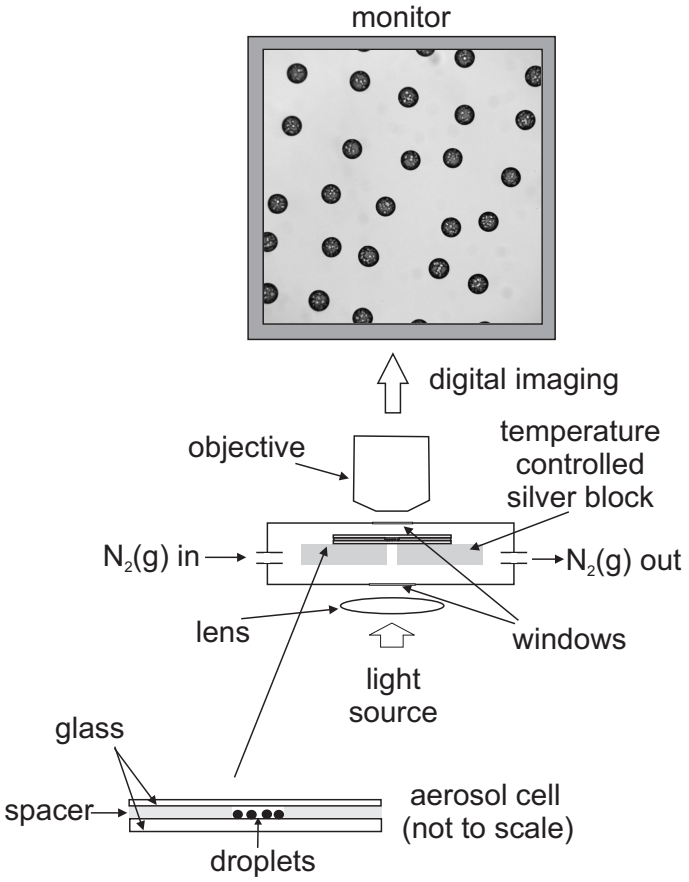

Figure 12: A sketch of the experimental setup used to study homogeneous and heterogeneous ice nucleation. It consists of a cryo-cooling stage attached to an optical microscope. An enlarged view of the closed aerosol cell is given which is placed within the cryo-cooling stage. The particle image shows melting of frozen $(NH_4)_2SO_4$ - H_2O particles. (Figure adapted from Knopf and Lopez, 2009)

0.1 K min^{-1}, and the deviation of $T_{\rm stage}$ from $T_{\rm ice}^{\rm melt}$ was found to be less than 0.05. Following that, the deliquescence relative humidities (DRHs) of K_2CO_3 (43.2%), K_2SO_4 (97.6%), LiCl (11.3%), $(NH_4)_2SO_4$ (80.0%) were measured for multiple samples by applying the calibrated T_{stage} and $T_{\rm dew}$. The relative humidity was changed at a rate of 0.6% RH min^{-1} which corresponds to a decreasing of $T_{\rm stage}$ by 0.1 K min^{-1}. There was no significant difference between observed and literature values of various inorganic salts over a wide range of RH values showing excellent agreement as shown in the Table 4. From our results it was shown that the uncertainty associated with $a_{\rm w}$ was less than 0.01 over our temperature range. The temperature of the cryo-cooling stage was then calibrated by measuring the melting points of heptane (182.60 K), octane (216.33 K), decane (243.55 K), dodecane (263.58 K) and ice

Table 4: Composition of aqueous multicomponent organic and inorganic/organic droplets employed in ice nucleation experiments.

Compound	DRH^{obs} (%)	DRH^{lit} (%)
K_2CO_3	43.4 ± 0.3	43.2 ± 0.5
K_2SO_4	97.5 ± 0.4	97.6 ± 0.3
LiCl	11.0 ± 0.1	11.3 ± 0.3
$(NH_4)_2SO_4$	80.1 ± 0.7	80.0 ± 1.5

(273.15 K). The results confirmed that the temperature sensor of the cryo-cooling stage was linear for the range of 170-280 K to within less than 0.1 K. Both optical microscopy set-ups were calibrated using a stage micrometer to determine the actual size of the particles observed.

3.6 Determination of Surface Area

Surface area is a key component in the analysis of heterogeneous ice nucleation. Two techniques are employed to quantify the surface area of Pahokee Peat and Leonardite contained within the droplets of the experiment. One technique involved taking pictures of aqueous Pahokee Peat and Leonardite droplet with a scanning electron microscope (SEM). Preparation of samples for SEM and optical microscopy examination are as follows. A solution identical to the specifications of Table 3 was prepared except that $(NH_4)_2SO_4$ was not added, and thus it consisted only of Pahokee Peat and Leonardite filtered and H_2O was then allowed to evaporate only leaving behind particles on the substrate. This solution was loaded into the single drop dispenser and deposited onto a silica nitrate substrate.

Table 5: Surface Area Analysis, based on geometric approximation from SEM images and BET measurements.

Method	Leonardite	Pahokee Peat
SEM Quantification	6.6×10^{-7} (cm^2)	1.2×10^{-5} (cm^2)
BET method	4.838 (m^2/g)	9.022 (m^2/g)
BET approximation	7.6×10^{-7} (cm^2)	1.4×10^{-6} (cm^2)

Images of a Leonardite droplet are shown in Figure 13 and 14. Figure 14 shows a small area of the sample where geometric approximation an surface area value was quantified.

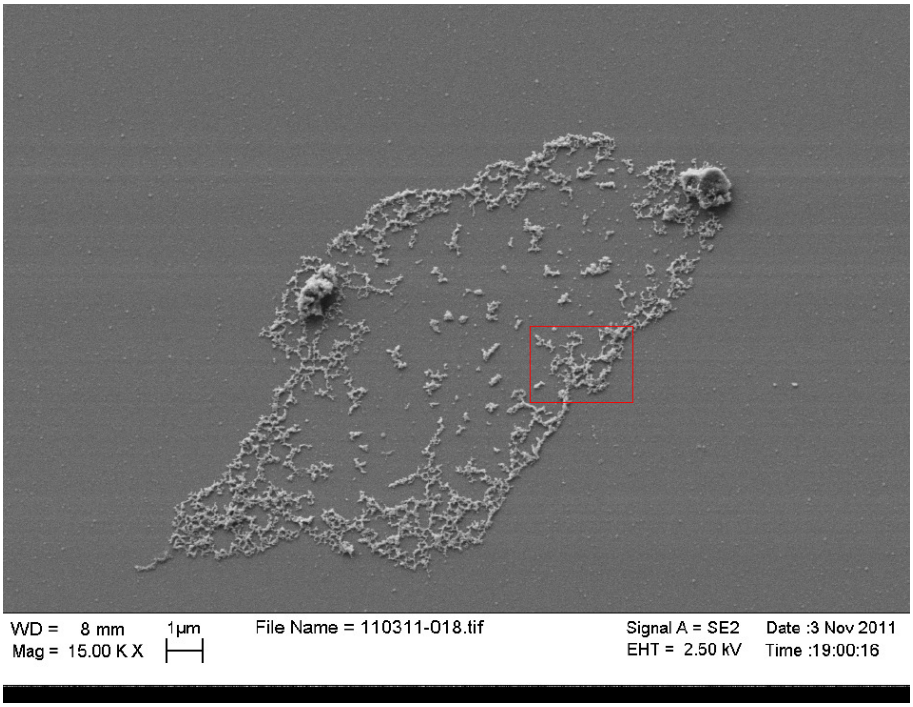

Figure 13: Leonardite droplet with 15,000x magnification

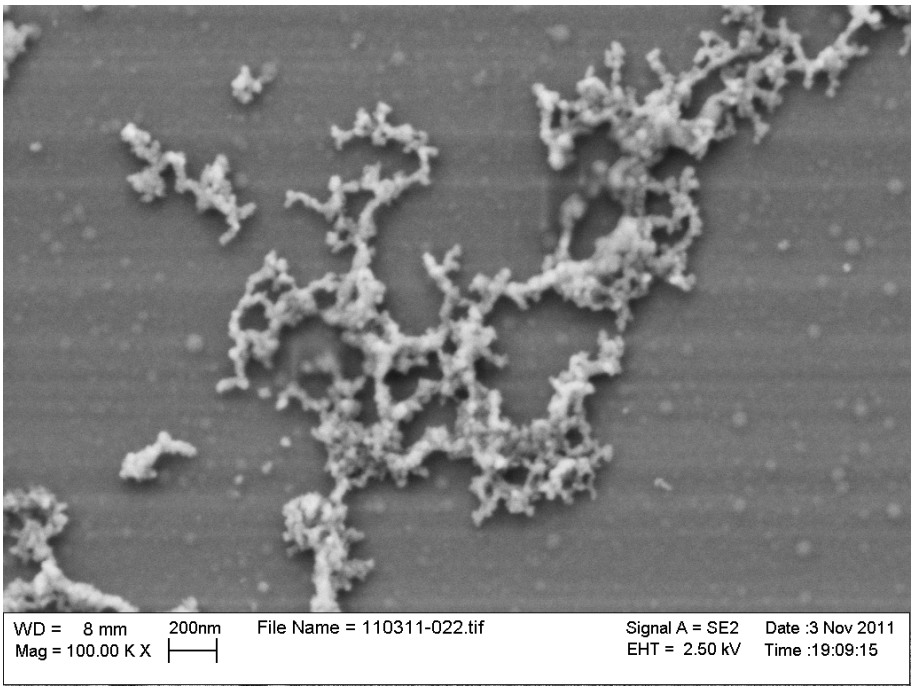

Figure 14: Scanning Electron Microscope Leonardite droplet with 100,000x magnification.

This was then scaled up as in according in Figure 13 to acquire a comprehensive surface area value representative of the particles contained within a droplet. The subsequent technique

was applied to Pahokee Peat droplets and the values are shown in Table 5. The structure of the Leonardite along with the sharp contrast against the substrate made the surface far easier to calculate as oppose to Pahokee Peat, this is most likely the cause for such a major difference in surface area values between the two. Surface area was also quantified using

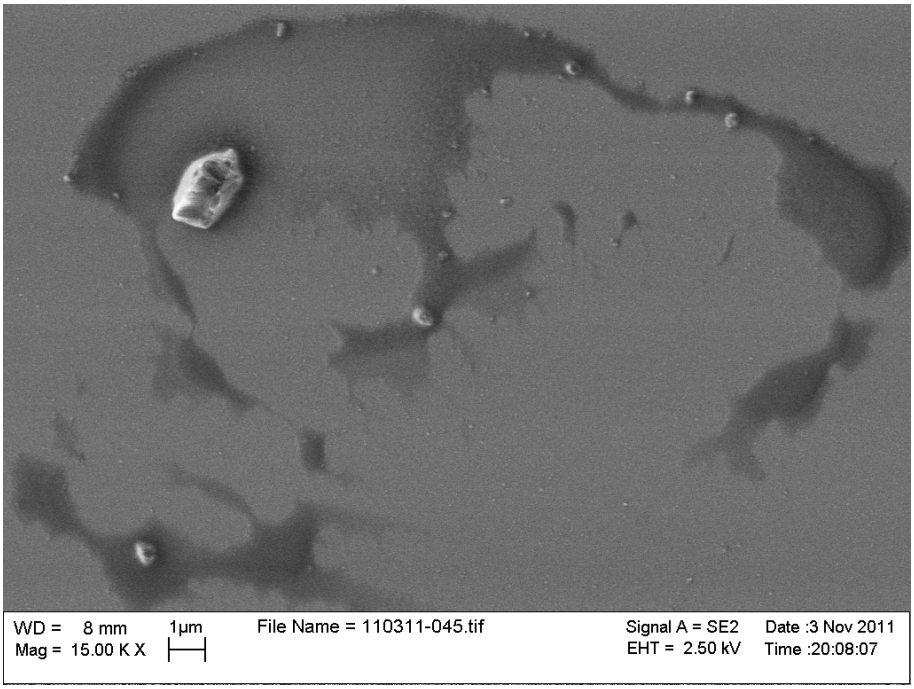

Figure 15: Scanning Electron Microscope Pahokee Peat droplet with 15,000x magnification.

the Brunauer, Emmett, Teller (BET) method (Brunauer et al., 1938). The BET method works based on the adsorption of gas molecules onto the solid surface, which quantifies the surface area of the material per mass. Both Pahokee peat and Leonardite preparation for the BET instrument involved crushing the appropriate substrate using a mortar and pestle, using the technique employed in preparing the solution from which droplets were created. However, because it was not possible to filter out the larger particles as was done in the experimental solution preparation, therefore it was assumed that roughly 25% of the particles mass remains in solution after filtering. This procedure yields a surface area value per droplet, as shown in Table 5 as BET approximation. Due to the similarity in values between the SEM quantification method and the BET approximation method for Leonardite, it was assumed that the BET method was the best fit to represent the surface area values used in the study.

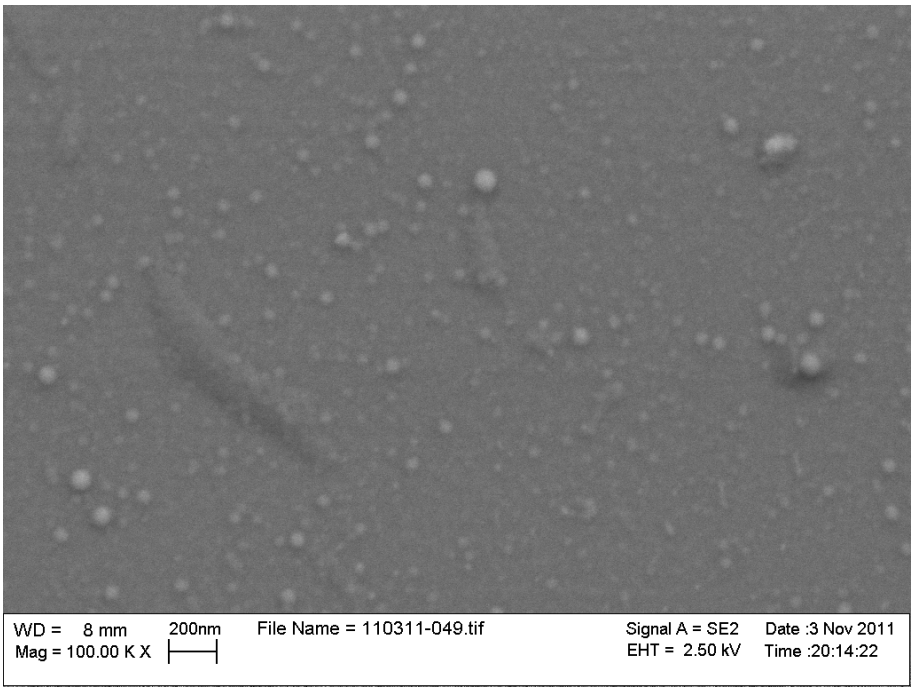

Figure 16: Scanning Electron Microscope Pahokee Peat droplet with 100,000x magnification.

3.7 Chemicals

N_2 (99.999%) was purchased from Praxair. All chemicals were purchased from VWR. Listed below are the chemicals and the corresponding purities used in our studies: LiCl (99.995%), $(NH_4)_2SO_4$ (99.95%), K_2CO_3 (99.997%), K_2SO_4 (99.99%), levoglucosan (99%), 4-hydroxybenzoic acid (99%), D-(+)-mannose (99%), D-(+)-galactose (98%), syringic acid (98+%), vanillic acid (98%), decane (99%), dodecane (99+%), octane (98+%), heptane (99+%). Leonardite and Pahokee peat were obtained from the International Humic Substance Society (IHSS). Millipore water (resistivity $>$ 18.2 MΩ cm) was used for preparation of aqueous solutions.

4 Results and Discussion

4.1 Homogeneous Ice Nucleation

Freezing temperatures, T_{freeze}, and melting temperatures, T_{melt} of aqueous $(NH_4)_2SO_4$/ levoglucosan of mass ratio 1:1 are shown in Figure 17 as a function of a_{w}. a_{w} is set for the particle preparation conditions at temperatures of 290-293 K, and assumed not to change with decreasing temperature (Koop et al., 2000). The range in freezing temperature is larger compared to the corresponding melting temperature, which can be attributed to differences in a_{w} between samples, the uncertainty in a_{w}, the difference in droplet sizes, and heterogeneous ice nucleation events. An uncertainty in $a_{\mathrm{w}} \leq \pm$ 0.01 can result in about $\pm$ 1.5 and 4 wt % uncertainty in the concentration of aqueous $(NH_4)_2SO_4$ solutions at high and low a_{w}, respectively (Clegg et al., 1998; Knopf and Lopez, 2009). In aqueous levoglucosan solutions, this uncertainty in a_{w} can result in about $\pm$ 2 and 7 wt% uncertainty at high and low a_{w}, respectively (Knopf and Lopez, 2009). According to CNT, droplets of less volume will nucleate ice at lower temperatures (Pruppacher and Klett, 1997). Heterogeneous ice nucleation as a result of impurities in the aqueous solution or an imperfect hydrophobic coating of the glass substrate cannot be ruled out however, which would lead to higher freezing temperatures (Knopf and Lopez, 2009). In Figure 17 and subsequent figures within this subsection, predicted homogeneous ice nucleation temperatures were derived using KO00 (Koop et al., 2000).

Figure 18a and b shows the mean melting temperatures, $\overline{T}_{\mathrm{m}}$, with 1σ uncertainty and median freezing temperatures, T_{f}, with $10th$ and $90th$ percentiles derived from aqueous $(NH_4)_2SO_4$/levoglucosan solution droplets with an $(NH_4)_2SO_4$/levoglucosan mass ratio of 10:1 and 1:1 and 1:5 and 1:10, respectively. $\overline{T}_{\mathrm{m}}$ are in good agreement with the predicted melting curve $a_{\mathrm{w}}^{\mathrm{ice}}$. T_{f} with corresponding percentiles lying within the theoretical uncertainties, indicating that KO00 provides an appropriate description of a_{w} in the supercooled temperature regime (Koop et al., 2000). This implies that a_{w} for aqueous $(NH_4)_2SO_4$/ lev-

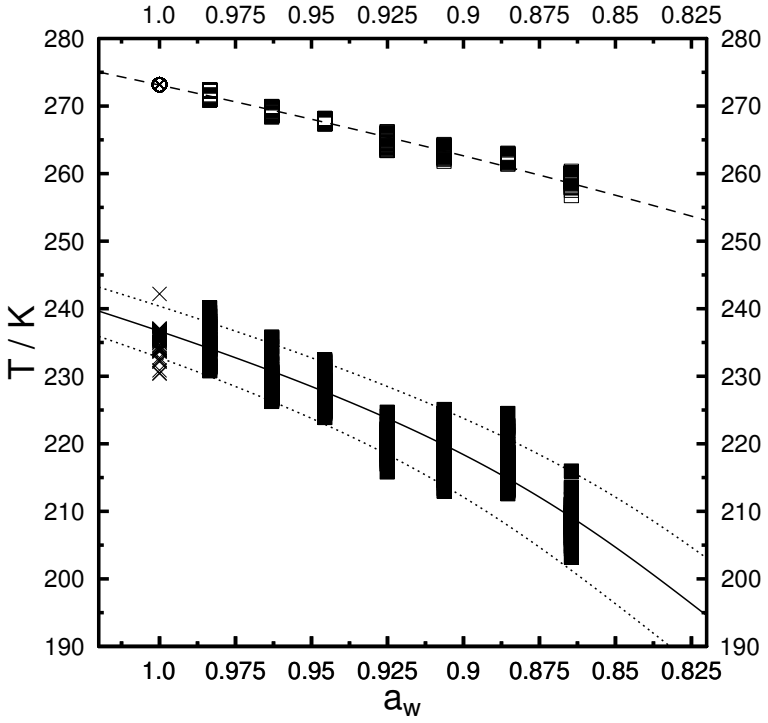

Figure 17: Temperature calibrated raw freezing and melting data of aqueous $(NH_4)_2SO_4$/levoglucosan droplets with a mass ratio of 1:1 given as filled and open squares, respectively, are shown as a function of a_w determined under particle preparation conditions. Freezing and melting points of pure water droplets are given as circled cross and crosses, respectively (Knopf and Lopez, 2009). Predicted melting and homogeneous freezing curves are plotted as dashed and solid lines, respectively (Koop et al., 2000). The homogeneous freezing curve represents J_{hom}=2.18×10^6 cm^{-3} s^{-1} to account for the larger droplets employed in this study (Koop et al., 2000). Dotted lines represent uncertainties in predicted freezing temperatures assuming an uncertainty in a_w of ±0.025 (Koop, 2004). It is assumed that a_w does not change with temperature (Koop et al., 2000).

oglucosan droplets does not change significantly with temperature.

Figure 18c shows the calculated mean melting and median freezing points from measurements of aqueous droplets composed of 6 major organic species typical of BBA, (mix 1) as given in Table 2. The data are plotted as a function of particle a_w, which was determined under preparation conditions. The melting temperatures are in agreement with expectations, however for low a_w freezing points are lower than predicted ones. Also shown in Figure 18c are $\overline{T}_m$ and T_f of levoglucosan droplets (Knopf and Lopez, 2009). Here it is observed that both mix 1 and levoglucosan exhibit shifts in a_w at low temperatures, however the shift in a_w between the two species is quite different at the melting point. (Knopf and Lopez, 2009).

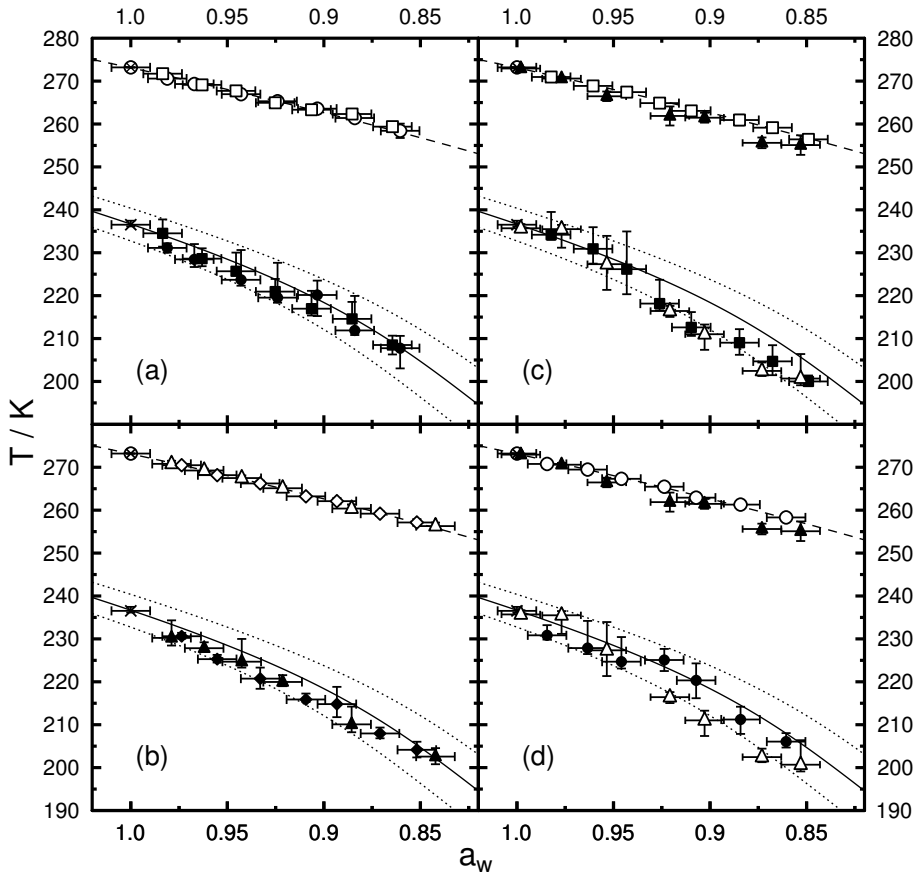

Figure 18: Experimentally derived median freezing and mean melting temperatures of aqueous $(NH_4)_2SO_4$/levoglucosan, mix 1, and mix 2 droplets. Error bars of freezing and melting data represent 10th and 90th percentiles and 1σ, respectively. Uncertainty in a_w is ± 0.01. Freezing and melting points of pure water droplets are given as crosses and circled crosses, respectively, with corresponding error bars. It is assumed that a_w does not change with temperature (Koop et al., 2000). Panel (a): aqueous $(NH_4)_2SO_4$/levoglucosan with a mass ratio of 10:1 and 1:1 are given as filled circles and open circles and filled squares and open squares, respectively. Panel (b): aqueous $(NH_4)_2SO_4$/levoglucosan droplets with a mass ratio of 1:5 and 1:10 are given as filled triangles and open triangles and filled diamonds and open diamonds, respectively. Panel (c): aqueous mix 1 and levoglucosan droplets are given as filled and open squares and open and filled triangles, respectively (Knopf and Lopez, 2009). Panel (d): aqueous mix 2 and levoglucosan droplets are given as filled and open circles and open and filled triangles, respectively (Knopf and Lopez, 2009). All other lines are the same as in Figure 17.

Figure 18d shows the melting and freezing points of aqueous inorganic/organic droplets as represented by mix 2 in Table 2 in addition to aqueous levoglucosan (Knopf and Lopez). Within the experimental and theoretical uncertainties, the experimentally observed $\overline{T}_m$ and T_f of mix 2 are in agreement with predictions. It is also observed that mix 2 droplets do not exhibit a shift in a_w as does mix 1 and aqueous levoglucosan (Knopf and Lopez, 2009).

Based on the data presented in this figure, it is clear that the addition of a minor fraction of $(NH_4)_2SO_4$ to aqueous organic droplets reduces the temperature dependency of a_w.

Homogeneous nucleation rate coefficients J_{hom} are derived from experimental data using the following formula:

$$J_{hom}\left(T^i\right) = \frac{n^i_{nuc}}{t^i_{tot} \cdot V^i} \ , \tag{26}$$

where n^i_{nuc} is the number of freezing events, and $t^i_{tot} \cdot V^i$ is the product of the total observation time and the available volume, respectively, in the i^{th} temperature interval. The product $t^i_{tot} \cdot V^i$ is the sum of the contribution from the droplets that remain liquid and those that freeze according to

$$t^i_{tot} \cdot V^i = \frac{\Delta T}{r} V^i_{rm} + \sum_{j=1}^{n^i_{nuc}} \frac{1}{r}\left(T^i_{st} - T^i_{nuc,j}\right) V^i_j \ , \tag{27}$$

where r is the experimental cooling rate, V^i_{rm} is the total droplet volume remaining until the end of the temperature interval, T^i_{st} is the start of the temperature interval, and $T^i_{nuc,j}$ and V^i_j are the freezing temperature and corresponding volume, respectively, of the j^{th} droplet nucleating ice within the i^{th} interval. Derivations of $J_{hom}(T^i)$ employ $\Delta T = 0.2$ K corresponding to our total experimental error in determining the temperature. Shown in Figure 19 are the derived J_{hom} values as a function of T and a_w for aqueous $(NH_4)_2SO_4$/levoglucosan, mix 1, and mix 2 droplets. All droplets employed in the study are used, demarcated by circles with colors corresponding to the appropriate a_w. For each droplet composition and a_w, J_{hom} increases strongly with decreasing T regardless of the $(NH_4)_2SO_4$ to levoglucosan mass ratio. Also shown in Figure 19a are the predicted J_{hom} values for a_w 0.981 and 0.861, which are in agreement with experimentally derived values when accounting for the uncertainty in KO00 of ± 0.025 to ± 0.05 (Koop et al., 2000).

Values of J_{hom} at the median freezing temperatures are shown in Figure 20 as a function of T and a_w for the following aqueous solutions: $(NH_4)_2SO_4$/levoglucosan droplets with

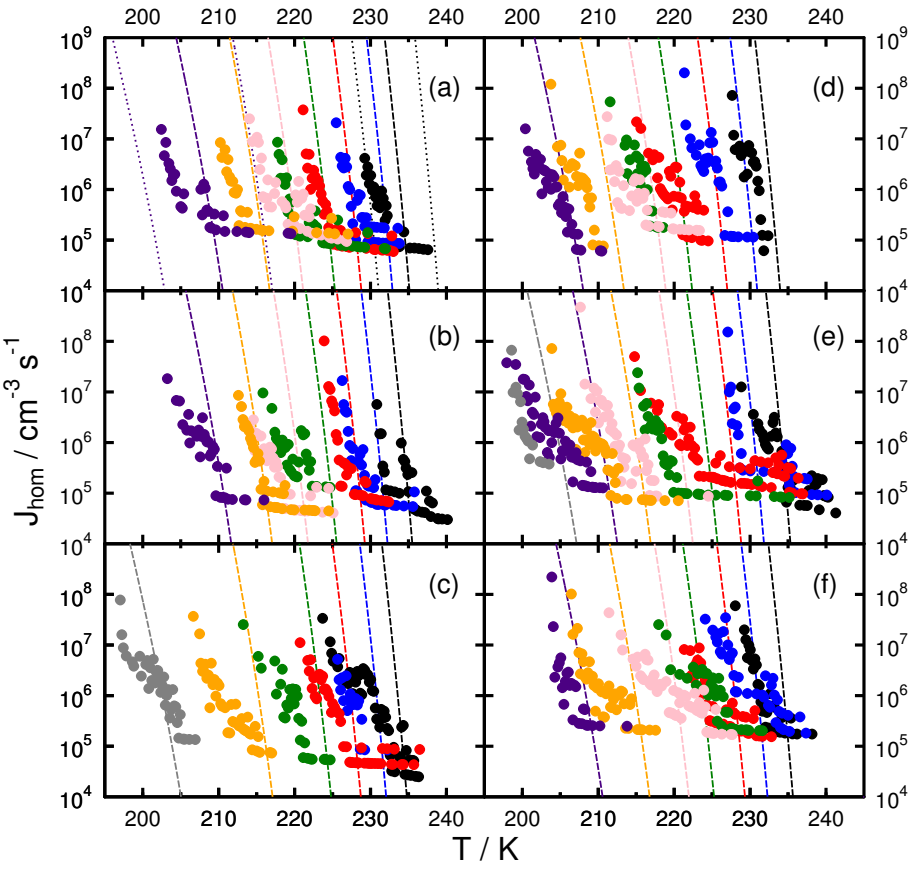

Figure 19: Experimentally derived homogeneous ice nucleation rate coefficients, J_{hom} shown as a function of T and a_{w} for aqueous droplets with mass ratios of 10:1, 1:1, 1:5, 1:10 and aqueous mix 1 and mix 2 in panels (a), (b), (c), (d), (e), and (f), respectively. Dashed lines represent corresponding predictions of J_{hom} (Koop et al., 2000) . Panel (a) black, blue, red, green, pink, orange, and indigo circles and dashed lines correspond to initial aw of 0.981, 0.967, 0.943, 0.924, 0.903, 0.884, and 0.861, respectively. Colored dotted lines represent uncertainty range of respective predicted Jhom values due to changes in a_{w} by $\pm$0.025 (Koop et al., 2000). Panel (b) black, blue, red, green, pink, orange, and indigo circles and dashed lines correspond to initial a_{w} of 0.984, 0.963, 0.946, 0.925, 0.906, 0.885, and 0.865, respectively. Panel (c) black, blue, red, green, orange, and gray circles and dashed lines correspond to initial a_{w} of 0.979, 0.962, 0.943, 0.921, 0.886, and 0.842, respectively. Panel (d) black, blue, red, green, pink, orange, and indigo circles and dashed lines correspond to initial a_{w} of 0.974, 0.955, 0.933, 0.909, 0.893, 0.871, and 0.852, respectively. Panel (e) black, blue, red, green, pink, orange, indigo, and gray circles and dashed lines correspond to initial a_{w} of 0.982, 0.961, 0.943, 0.926, 0.910, 0.885, 0.868 and 0.849, respectively. Panel (f) black, blue, red, green, pink, orange, and indigo circles and dashed lines correspond to initial a_{w} of 0.984, 0.963, 0.946, 0.924, 0.907, 0.884, and 0.861, respectively.

mass ratios of 10:1, 1:1, 1:5, 1:10, and mix 1, mix 2, $(NH_4)_2SO_4$, levoglucosan, water, and NaCl droplets (Knopf and Lopez, 2009; Alpert et al., 2011). All data points lay within the uncertainty of KO00 with the exception of an aqueous levoglucosan data point and 2 NaCl points (Knopf and Lopez, 2009; Alpert et al., 2011). Aqueous levoglucosan droplets have been

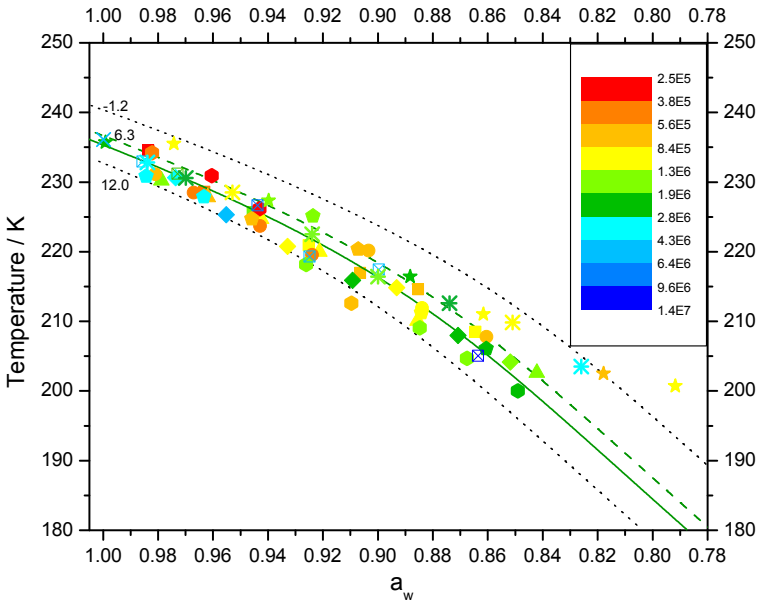

Figure 20: Experimentally derived J_{hom} values determined at median freezing temperatures as a function of temperature and a_{w}. Circles, squares, triangles, and diamonds represent ice nucleation data from aqueous $(NH_4)_2SO_4$/levoglucosan droplets with mass ratios of 10:1, 1:1, 1:5, and 1:10, respectively. Hexagons and pentagons represent ice nucleation data from aqueous mix 1 and mix 2 droplets, respectively. Aqueous levoglucosan and $(NH_4)_2SO_4$ droplets are given as stars and crossed squares, respectively (Knopf and Lopez, 2009). Aqueous NaCl droplets are represented as asterisks (Alpert et al., 2011). Water droplets are represented as crosses. The color coding gives the homogeneous ice nucleation rate coefficient in units $\mathrm{cm}^{-3}\ \mathrm{s}^{-1}$. The solid and dashed green lines represent experimentally derived and predicted homogeneous freezing curves, respectively.

observed to deviate significantly from preparation a_{w} at lower T (Knopf and Lopez, 2009). Aqueous NaCl droplets have been observed to form NaCl $\cdot$ $2H_2O$ at a a_{w} of 0.806 (Koop et al., 2000a; Alpert et al., 2011). J_{hom} of all the aqueous solutions except levoglucosan and mix 1 was obtained at T_{f} for all a_{w} except NaCl at 0.806 were averaged to produce $J_{\mathrm{hom}}^{\mathrm{avg}} = 2.18 \times 10^6\ \mathrm{cm}^{-3}s^{-1}$. This corresponds to a Δa_{w} shift of 0.2984 in calculated from Eq. 15. The uncertainty in KO00 of ± 0.025 to ± 0.05 is shown in Fig. 20 with corresponding J_{hom} values, which span ± 6 orders of magnitude. The data compiled experimentally only spans ± 1 order of magnitude, indicating KO00 overpredicts $\mathrm{J_{hom}}$ values significantly.

4.2 Heterogeneous Ice Nucleation

Median freezing temperatures of aqueous $(NH_4)_2SO_4$ droplets containing Leonardite are shown in Fig. 21a as a function of T, a_w and wt% determined at droplet preparation conditions. Within the experimental uncertainty, melting temperatures of aqueous $(NH_4)_2SO_4$ droplets containing Leonardite are in good agreement with the predicted melting curve, a_w^{ice}. T_f^{leo} are 5 to 15 K warmer than the homogeneous freezing curve at high and low a_w, respectively, as shown in Fig. 21a. The freezing curve $a_w^{f,het}$ is constructed according to Equation 15 by fitting T_f^{leo}, where $\Delta a_{w,het}$ is the only free parameter. The best fit yields $\Delta a_{w,het}^{leo} = 0.2673$ and is in good agreement with T_f^{leo}, as indicated by the grey line in Fig. 21a. Deviations of T_f^{leo} from predictions can be attributed to differences in a_w between samples and the uncertainty in a_w (Koop, 2004; Knopf and Lopez, 2009).

Median freezing temperatures of aqueous $(NH_4)_2SO_4$ droplets containing Pahokee Peat are shown in Fig. 21b as a function of T, a_w and wt% determined at droplet preparation conditions. Within the experimental uncertainty, melting temperatures of aqueous $(NH_4)_2SO_4$ droplets containing Pahokee Peat are in good agreement with the predicted melting curve, a_w^{ice}. T_f^{pp} are 10 to 20 K warmer than the homogeneous freezing curve at high and low a_w, respectively, as shown in Fig. 21b. Pahokee Peat nucleates ice at a higher temperatures compared to Leonardite. The freezing curve $a_w^{f,het}$ is constructed according to Eq. **19** yields $\Delta a_{w,het}^{pp} = 0.2414$ which is within the error of T_f^{pp}, as indicated by the grey line in Fig. 21b. The results presented above indicate the modified water activity approach is sufficient to describe and predict immersion freezing temperatures of Leonardite and Pahokee Peat particles in aqueous $(NH_4)_2SO_4$ droplets.

Freezing data generated from this study were analyzed and plotted in a probability density histogram and cumulative distributions, as shown in Figs (22) and 23. The frozen fraction of droplets, f, was calculated from observations by $f = N_{ice}/N_{tot}$ where N_{ice} is the number of frozen droplets as a function of T, and N_{tot} is the total number of analyzed drops (Shaw et al., 2005). Collectively, these points represent a cumulative distribution as a function of

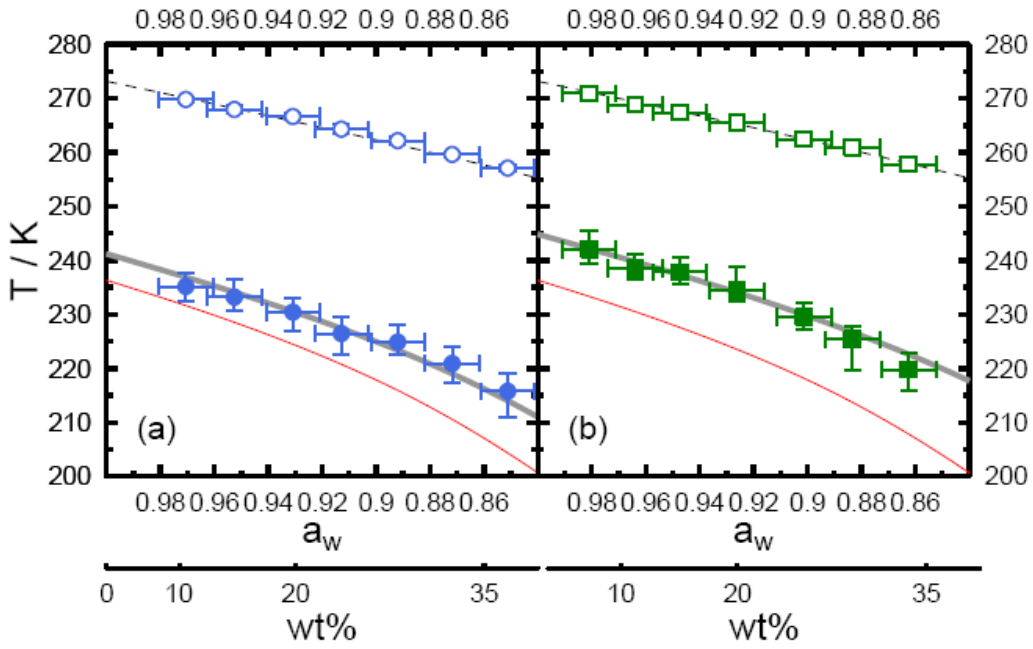

Figure 21: Median heterogeneous freezing temperatures and corresponding mean melting temperatures for (a) Leonardite and (b) Pahokee Peat particles immersed in aqueous $(NH_4)_2SO_4$ droplets are shown as solid and open circles, and solid and open squares respectively, as a function of a_w and wt%. The error bars for the freezing temperatures indicate the 10th and 90th percentiles and error bars for the melting temperatures indicate one standard deviation. Uncertainty in a_w is ± 0.01. The black dashed and red solid line represent the predicted ice melting curve and homogeneous freezing curve (Koop et al., 2000). The solid gray line represent a shift of the melting curve by $\Delta a_{w,het}^{leo} = 0.2673$ and $\Delta a_{w,het}^{pp} = 0.2414$. It is assumed that a_w of the aqueous droplets does not change with temperature (Koop et al., 2000).

T. The probability density histogram (PDH) binned in 1.0 K increments was normalized to N_{tot}. The spread in freezing temperatures can once again be explained by uncertainties in a_w (Koop, 2004) at low T in addition to homogeneous freezing events.

Here, we derive heterogeneous ice nucleation rate coefficient, J_{het} for all experimentally acquired data according to the equation:

$$J_{het}\left(T^i\right) = \frac{n_{nuc}^i}{t_{tot}^i \cdot A^i} \ , \tag{28}$$

where n_{nuc}^i and $t_{tot}^i \cdot A^i$ is the number of freezing events, and the product of the total observation time and the available IN surface area, respectively, in the i^{th} temperature interval. The product $t_{tot}^i \cdot A^i$ is the sum of the contribution from the droplets that remain liquid and

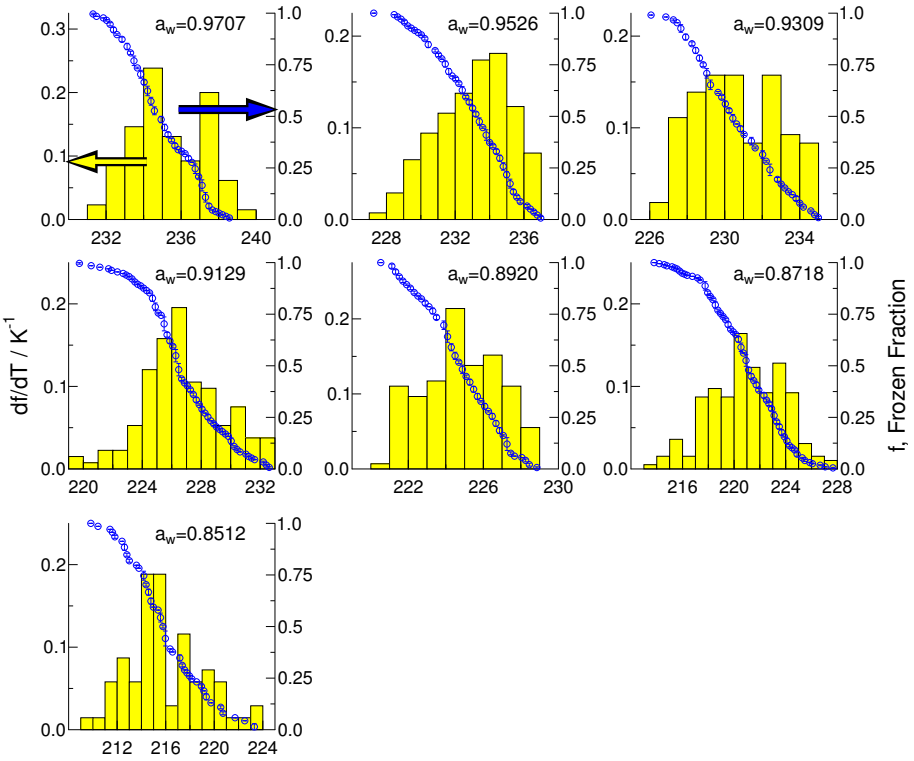

Figure 22: Summary of all observed immersion freezing events with Leonardite particles as a function of a_{w} and T. The frozen fraction, f, of droplets in 0.2 K temperature increments is represented by blue circles. Error bars indicate the range of f in a temperature increment of 0.2 K. Yellow bars show the probability density histogram (PDH) binned in 1.0 K increments. For each panel, a_{w} is given. The values for the PDH are given on the left y-axis and f on the right y-axis.

those that freeze according to

$$t^i_{\mathrm{tot}} \cdot A^i = \frac{\Delta T}{r} A^i_{\mathrm{rm}} + \sum_{j=1}^{n^i_{\mathrm{nuc}}} \frac{1}{r} \left(T^i_{\mathrm{st}} - T^i_{\mathrm{nuc},j} \right) A^i_j \ , \tag{29}$$

where r is the experimental cooling rate, A^i_{rm} is the total surface area remaining until the end of the temperature interval, T^i_{st} is the start of the temperature interval, and $T^i_{\mathrm{nuc},j}$ and A^i_j are the freezing temperature and corresponding IN surface area, respectively, of the j^{th} droplet nucleating ice within the i^{th} interval. Derivations of $J_{\mathrm{het}}(T^i)$ employ $\Delta T = 0.2$ K corresponding to our total experimental error in determining the temperature.

Figure 24 shows experimentally derived J_{het} as a function of T and initial a_{w}. For each droplet a_{w}, J_{het} increases exponentially with decreasing T. For a given a_{w}, such as 0.9707, a change in 10 K results in a change in J_{het} of over 2 orders of magnitude. Using experimentally

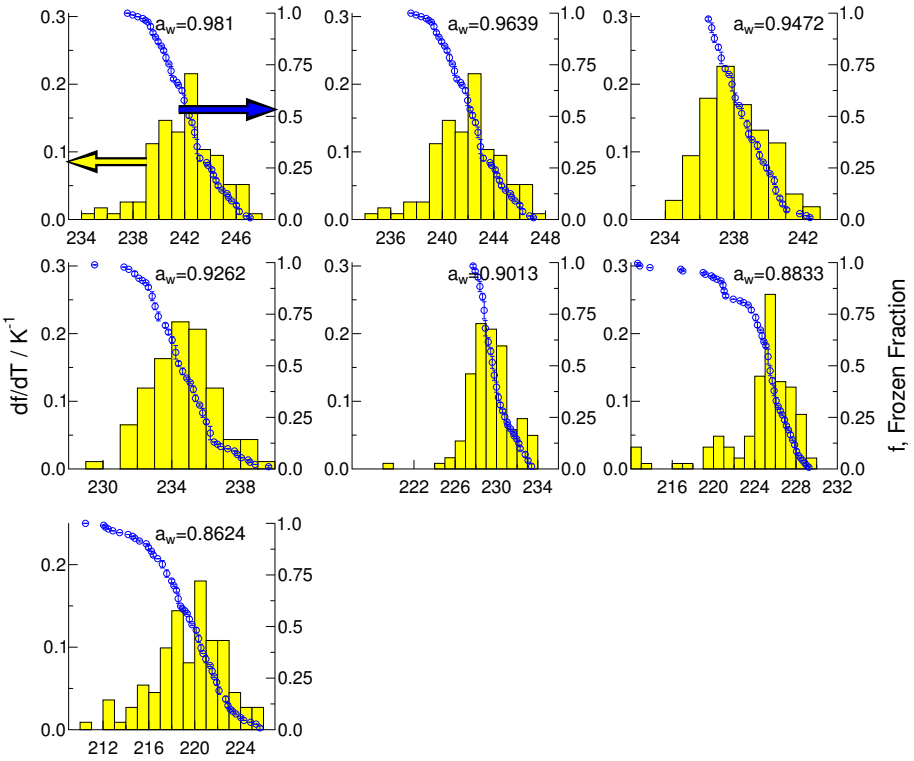

Figure 23: Summary of all observed immersion freezing events with Pahokee Peat particles as a function of a_{w} and T. The frozen fraction, f, of droplets in 0.2 K temperature increments is represented by blue circles. Error bars indicate the range of f in a temperature increment of 0.2 K. Yellow bars show the probability density histogram (PDH) binned in 1.0 K increments. For each panel, a_{w} is given. The values for the PDH are given on the left y-axis and f on the right y-axis.

derived values of J_{het}, contact angles are derived according to Eq. 13. As mentioned above, an α value of 180° implies the IN has no impact on the nucleating abilities of the bulk phase. In Figure 25, we see there is a strong dependence with temperature. For a given a_{w}, a change of 10 K results in a change in roughly 20° in α. Furthermore, we observe that thermodynamic properties, such as a_{w} and T have a strong influence on α.

A time independent analysis of the data results in the derivation of the cumulative and differential ice nuclei spectra as shown in Figs. 24b as a function of T and a_{w}. As in the case of J_{het}, both K and k increase significantly with decreasing temperature. Also important to note are the similarities in the values of J_{het}, and K, indicating that K may also be parameterized by $\Delta a_{\mathrm{w,het}}^{\mathrm{leo}}$. As the temperature decreases for a given a_{w}, α increases, reducing the necessary energy barrier for ice nucleation to occur.

Figure 26 shows experimentally derived J_{het} for Pahokee Peat as a function of T and

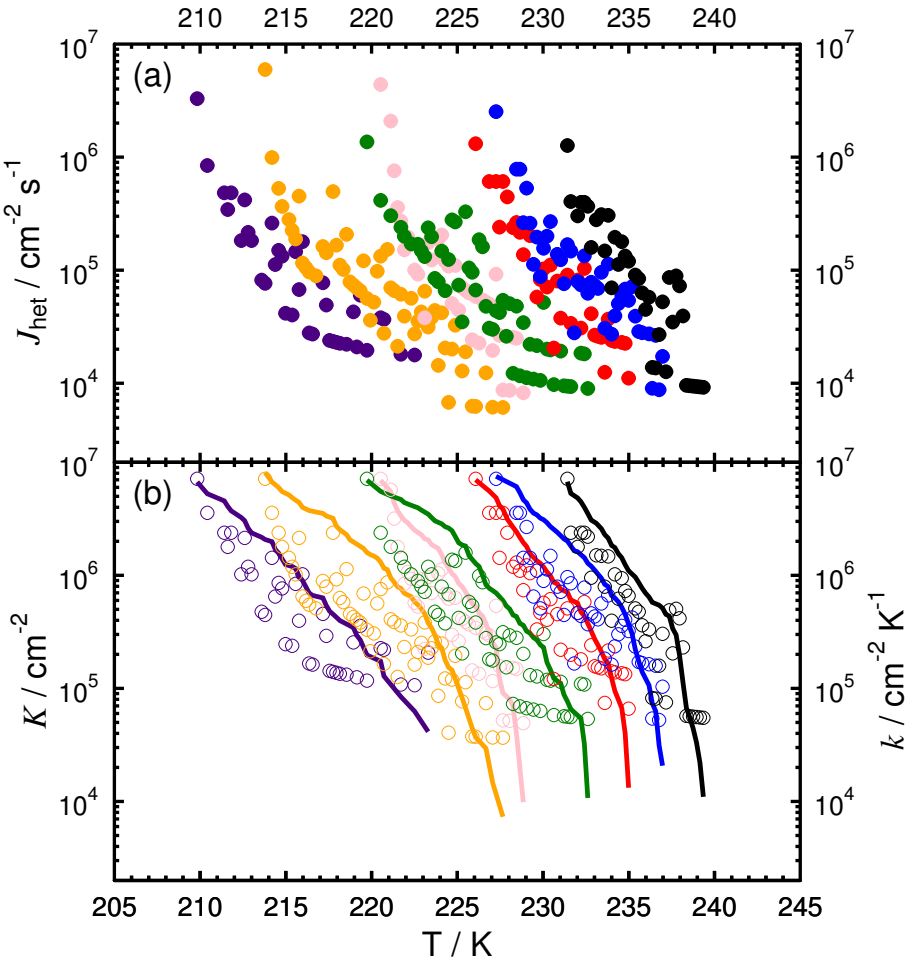

Figure 24: Panel (a) and panel (b) show experimentally derived heterogeneous ice nucleation rate coefficients, J_{het}, K, and k shown as a function of T and a_w. Black, purple, blue, green, red, teal, and pink circles correspond to aqueous $(NH_4)_2SO_4$ droplets containing Leonardite with initial a_w of 0.9707, 0.9526, 0.9309, 0.9129, 0.8920, 0.8718, and 0.8512 respectively.

initial a_w. For each droplet a_w, J_{het} increases exponentially with decreasing T. For a given a_w, such as 0.981, a change of 10 K results in a change in J_{het} of over 2 orders of magnitude. With experimentally derived values of J_{het}, contact angles are derived and shown in Fig. 27. In Fig. 27, we see there is a strong dependence with temperature. For a given a_w, a change in 10 K results in a change in roughly 20° in α. Once again it is observed that thermodynamic properties, such as a_w and T have a strong influence on α. As the temperature decreases for a given a_w, α increases, facilitating ice nucleation.

A time independent analysis of the data results in the derivation of the cumulative and differential ice nuclei spectra as shown in Fig. 26 as a function of T and a_w. As in the case

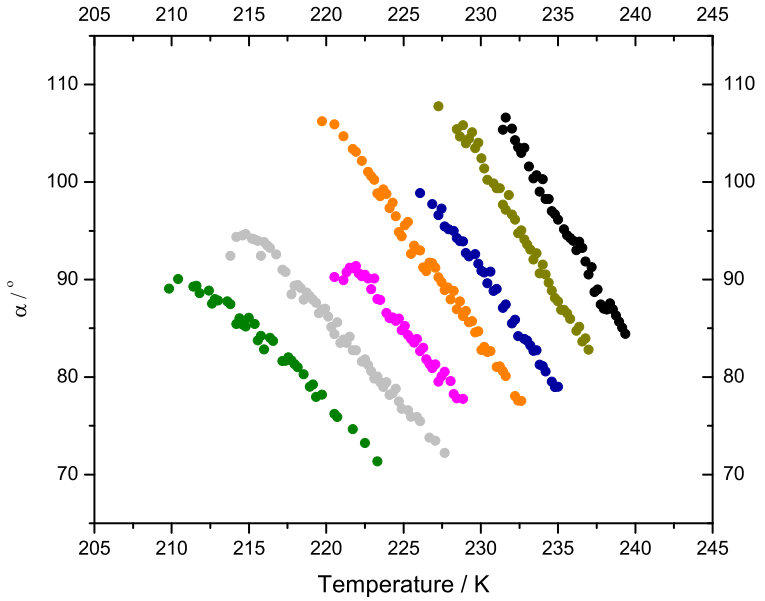

Figure 25: Contact angles, α, calculated from experimental values of J_{het} as a function of T. Black, yellow, blue, orange, pink, grey, and green circles correspond to aqueous $(NH_4)_2SO_4$ droplets containing Leonardite with initial a_{w} values of 0.9707, 0.9526, 0.9309, 0.9129, 0.8920, 0.8718, and 0.8512 respectively.

of J_{het}, K and k they all increase significantly with decreasing temperature. Also important to note are the similarities in the values of J_{het}, and K, indicating that K may also be parameterized by $\Delta a_{\text{w,het}}^{\text{pp}}$.

Table 6 shows J_{het}, $k(T)$, $K(T)$ calculated at the median T_{f}, contrasting the nucleating abilities of Pahokee Peat versus that of Leonardite based on the parameter S_{ice}. A general trend is observed in which K is roughly 1 order of magnitude larger than J_{het} across all water activities and temperature regimes.

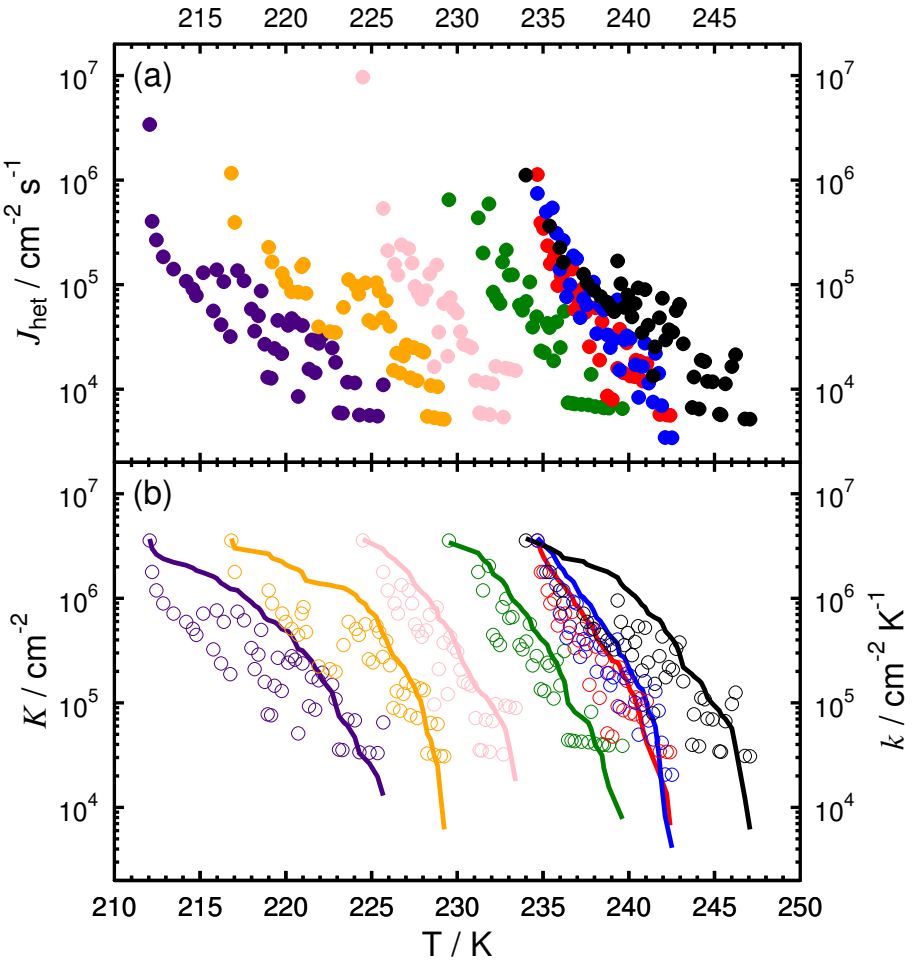

Figure 26: Panel (a) and panel (b) show experimentally derived heterogeneous ice nucleation rate coefficients, J_{het}, K, and k shown as a function of T and a_w. Black, purple, blue, green, red, teal, and pink circles correspond to aqueous $(NH_4)_2SO_4$ droplets containing Pahokee Peat with initial a_w of 0.981, 0.9639, 0.9472, 0.9262, 0.9013, 0.8833, and 0.8624 respectively.

5 Atmospheric Implications

5.1 Homogeneous Ice Nucleation

The experimental homogeneous ice nucleation data obtained in this study indicate that for organic particles with fixed compositions, a minor fraction of $(NH_4)_2SO_4$ decreases the temperature dependency of a_w in the supercooled region. This phenomenon is important in calculating the liquid content of an aqueous drop. For example, a pure aqueous levoglucosan particle for which a_w decreases with decreasing temperature will take up significantly more water at lower temperatures in order to remain in equilibrium with the surrounding

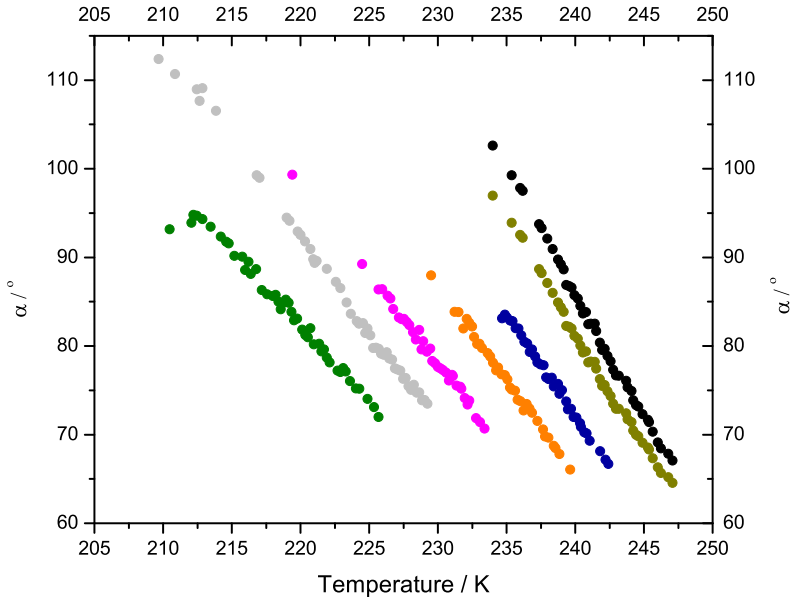

Figure 27: Contact angles, α, calculated from experimental values of J_{het} as a function of T. Black, yellow, blue, orange, pink, grey, and green correspond to aqueous $(NH_4)_2SO_4$ droplets containing Pahokee Peat with initial a_{w} values of 0.981, 0.9639, 0.9472, 0.9262, 0.9013, 0.8833, and 0.8624 respectively.

water partial pressure as inferred from its composition determined at higher temperatures. However, the findings here indicate that the presence of $(NH_4)_2SO_4$ within an aqueous organic droplet will nullify the change in a_{w} with T. This has serious implications for cloud condensation nuclei activation and ice nucleation via the immersion mode.

Experimental data also indicate that KO00 significantly overpredicts J_{hom} by up to 12 orders of magnitude, although the data presented here can constrain the predicted J_{hom} value to 2 orders of magnitude. Even so when applied to an atmospheric setting, the impact can be significant. Calculating the ice particle production rates can be calculated from the equation

$$P_{\text{het}}^{\text{ice}}(T, \text{RH}) = J_{\text{hom}}(T, RH) \cdot V_{\text{droplet}} \ , \tag{30}$$

where V_{droplet} is the droplet volume, for example shows that differences of 2 orders of magnitude in J_{hom} can result in 2 orders of magnitude difference in ice particle production rates.

Table 6: Summary of heterogeneous ice nucleation parameters evaluated at median freezing temperatures for Leonardite and Pahokee Peat given in the top and bottom panel, respectively.

a_{w}	0.971	0.953	0.931	0.913	0.892	0.872	0.851
$T_{\mathrm{f}}^{\mathrm{leo}}\,\mathrm{K}^{-1}$	235.2	233.2	230.4	226.5	224.9	220.9	215.8
$T_{\mathrm{m}}^{\mathrm{leo}}\,\mathrm{K}^{-1}$	269.8	268.0	266.7	264.3	262.2	259.6	257.1
$S_{\mathrm{ice}}(T_{\mathrm{f}}^{\mathrm{leo}})$	1.40	1.40	1.40	1.43	1.41	1.42	1.44
$J_{\mathrm{het}}(T_{\mathrm{f}}^{\mathrm{leo}}) \times 10^4\,\mathrm{cm}^{-2}\,\mathrm{s}^{-1}$	10.2	6.7	7.1	10.6	7.8	9.6	10.5
$k(T_{\mathrm{f}}^{\mathrm{leo}}) \times 10^5\,\mathrm{cm}^{-2}\,\mathrm{K}^{-1}$	5.1	5.6	1.2	2.8	6.3	8.7	10.2
$K(T_{\mathrm{f}}^{\mathrm{leo}}) \times 10^5\,\mathrm{cm}^{-2}$	9.7	9.4	8.7	8.3	9.7	11.0	9.0
a_{w}	0.981	0.964	0.947	0.926	0.901	0.883	0.862
$T_{\mathrm{f}}^{\mathrm{pp}}\,\mathrm{K}^{-1}$	242.1	238.6	237.9	234.4	229.5	225.4	219.8
$T_{\mathrm{m}}^{\mathrm{pp}}\,\mathrm{K}^{-1}$	270.9	268.8	267.4	265.5	262.5	261.0	257.8
$S_{\mathrm{ice}}(T_{\mathrm{f}}^{\mathrm{pp}})$	1.33	1.34	1.33	1.35	1.37	1.40	1.41
$J_{\mathrm{het}}(T_{\mathrm{f}}^{\mathrm{pp}}) \times 10^4\,\mathrm{cm}^{-2}\,\mathrm{s}^{-1}$	4.7	4.4	5.8	5.4	5.5	7.7	3.8
$k(T_{\mathrm{f}}^{\mathrm{pp}}) \times 10^5\,\mathrm{cm}^{-2}\,\mathrm{K}^{-1}$	1.7	1.8	5.1	2.8	4.3	2.7	2.4
$K(T_{\mathrm{f}}^{\mathrm{pp}}) \times 10^5\,\mathrm{cm}^{-2}$	4.8	4.8	5.5	4.7	4.9	4.6	4.8

5.2 Heterogeneous Ice Nucleation

There are very few studies which directly measure the ice nuclei concentration in clouds due to biomass burning. A few studies have explored ice nuclei as a result of controlled biomass burning within laboratory settings , however the concentrations of IN implemented are not atmospherically relevant (Petters et al., 2009; Demott et al., 2009). A field study involving the characterization of HULIS quantities from a biomass burning event observed concentrations in the range of 5.9 - 18.1 μg m^{-3}. The density of HULIS were found to be roughly 1.50 g m^{-3}, for a variety of samples, and hence will be assumed to be applicable in this case (Dinar et al., 2006). Here we assume a spherical orientation with an average diameter of 1 μm, which yields IN concentrations of roughly 7500 - 23000 L^{-1}. We will take the lower limit and further assume that only 0.1 % of total particles actually make it to heights in the atmosphere where ice formation occurs, yielding a value of 7.5 L^{-1}. Using

this value as our standard, the experimental values derived in this study will be related to atmospheric conditions.

Time dependent and time-independent methods used to quantify heterogeneous ice nucleation are different in their approach, and thus different in how they can be implemented in the atmospheric context. $J_{\rm het}$ may be used to calculate ice particle production rates, $P^{\rm ice}$ from the equation:

$$P^{\rm ice}_{\rm het}(T, {\rm RH}) = J_{\rm het}(T, {\rm RH}) \cdot A_{\rm particle} \ , \tag{31}$$

where $A_{\rm particle}$ is the particle surface area per unit volume of air. $P_{\rm ice}$ is a function of T, and RH. In the context of this study, $a_{\rm w}$ = RH. K can also be used to determine ice particle production as a function of temperature, independent of time as follows:

$$P^{\rm ice}_{\rm het}(T, {\rm RH}) = K(T, {\rm RH}) \cdot A_{\rm particle} \ . \tag{32}$$

For the purpose of calculating ice particle production, we assume we have a surface area similar to that found within our aqueous droplets of $7{\times}10^{-7}$ cm^2, which yields an $\rm A_{particle}$ value of 5.25 $\times 10^{-6}$ cm^2 L^{-1}. Suppose RH = 96% and T = 240 K and a corresponding $J_{\rm het}$ = $4.5{\times}10^4$ cm^{2}s^{-1}, we acquire $P^{\rm ice}_{\rm het}$ = 12 L^{-1} min^{-1}. Using the same conditions and assumptions for the time independent measurement, applying a value of $K = 4.8{\times}10^5$ cm^2 we arrive at $P^{\rm ice}_{\rm het}$ = 2 L^{-1}. As according to the calculations above, the time-dependent approach will always yield higher ice particle numbers with time compared to the time-independent approach under similar conditions. Consequently predictions of ice crystal production are sensitive to the whether the time-dependent or time-independent approach is used.

6 Summary and Outlook

Homogeneous and heterogeneous freezing and melting measurements of ice from surrogates of biomass burning aerosol have been acquired in the temperature range of 180 to 273 K for water activities of 0.85 to 0.98. Over 6000 individual droplets have been tested and analyzed in this study. Homogeneous freezing of aqueous organic droplets indicated that deviations in a_{w} in the supercooled region are negligible with the addition of $(NH_4)_2SO_4$. Homogeneous nucleation rates derived allowed for generation of corresponding ice particle production rates. Furthermore, the ice nucleation data presented in this study representing a wide range of different aqueous inorganic, organic, and inorganic/organic droplets corroborate the general validity of the water activity-based homogeneous ice nucleation theory. However, more studies are needed to explore the change in a_{w} with T from both organic and organic/inorganic mixtures.

Median heterogeneous freezing temperatures were analyzed by the modified water-activity based theory and found to be useful in describing the nucleating abilities of Leonardite and Pahokee Peat immersed in aqueous $(NH_4)_2SO_4$ by a shift in $\Delta a_{\mathrm{w}} = 0.2673$ and $\Delta a_{\mathrm{w}} = 0.2414$, respectively. It was determined that Pahokee Peat is a much more effective IN than Leonardite. Subsequent values of J_{het}, k, and K were determined for the two systems as a function of T and a_{w}. Finally the values obtained during this study were implemented into atmospheric scenarios which showed a significant difference in resulting ice particle numbers when using the time-dependent and time-independent approaches. More in situ measurments are needed, however for IN concentrations in the upper troposphere arising from biomass burning events to either validate or disprove the two approaches. Additionally, the role of immersion mode ice nucleation in aqueous organic droplets should be further investigated in order to determine whether there is also an observable shift in a_{w}, which will impact freezing temperatures as was in the case of homogeneous ice nucleation.

References

Albrecht, B. A.: Aerosols, cloud microphysics, and fractional cloudiness, Science, 245, 1227–1230, 1989.

Andreae, M. O. and Crutzen, P. J.: Atmospheric aerosols: biogeochemical sources and role in atmospheric chemistry, Science, 276, 1052–1058, 1997.

Baker, M. B.: Cloud microphysics and climate, Science, 276, 1072–1078, 1997.

Baker, M. B. and Peter, T.: Small-scale cloud processes and climate, Nature, 451, 299–300, 2008.

Clegg, S. L., Brimblecombe, P., and Wexler, A. S.: A thermodynamic model of the system, J. Phys. Chem. A, 102, 2155–2171,available at: http://www.aim.env.uea.ac.uk/aim/aim.php (last access: May 2010), 1998.

Forster, P., Ramaswamy, V., Artaxo, P., Berntsen, T., Betts, R., Fahey, D. W., Haywood, J., Lean, J., Lowe, D. C., Myhre, G., Nganga, J., Prinn, R., Raga, G., Schulz, M., and Van Dorland, R.: Changes in Atmospheric Constituents and in Radiative Forcing, in: Climate Change 2007: The Physical Science Basis. Contribution of Working Group I to the Fourth Assessment Report of the Intergovernmental Panel on Climate Change, chap. 2, edited by: Solomon, S., Qin, D., Manning, M., Chen, Z., Marquis, M., Averyt, K. B., Tignor, M., and Miller, H. L. Cambridge University Press, Cambridge, UK and New York, NY, USA, 131–234, 2007.

Iinuma, Y., Bruggemann, E., Gnauk, T., Muller, K.: Source characterication of biomass burning particles: The combustion of selected European conifer, African hardwood, savanna grass and German and Indonesian peat, J. Geo. Phys. Res., 112, D08209, 2007.

Knopf, D. A. and Lopez, M. D.: Homogeneous ice freezing temperatures and ice nucleation rates of aqueous ammonium sulfate and aqueous levoglucosan particles for relevant atmospheric conditions, Phys. Chem. Chem. Phys., 11, 8056–8068, 2009.

Knopf, D. A. and Rigg, Y. J.: Homogeneous ice nucleation from aqueous inorganic/organic particles representative of biomass burning: water activity, freezing temperatures, nucleation rates, J. Phys. Chem. A, 115, 762–773, http://dx.doi.org/10.1021/jp109171gdoi:10.1021/jp109171g, 2011.

Koop, T., Luo, B. P., Tsias, A., and Peter, T.: Water activity as the determinant for homogeneous ice nucleation in aqueous solutions, Nature, 406, 611–614, 2000.

Murphy, D. M., Cziczo, D. J., Hudson, P. K., Thomson, D. S.: Carbonaceous material in aersosol particles in the lower stratosphere and tropopause region, J. Geo. Phys. Res., 131, 1539–1565, 2007.

Murphy, D. M., Thomson, D. S., Mahoney, T. M.,.: In situ measurements of organics, meteoritic material, mercury, and other elements in aerosols at 5 to 19 kilometers, J. Science, 282, 1664–1669, 1998.

Prenni, A. J., Demott, P. J., Rogers, D. C., Kreidenweis, S. M., McFarquhar, G. M., Zhang, G., and Poellot, M. R.: Ice nuclei characteristics from M-PACE and their relation to ice formation in clouds, Tellus B, 61, 436–448, 2009.

Pruppacher, H. R. and Klett, J. D.: Microphysics of Clouds and Precipitation, Kluwer Academic Publishers, Dordrecht, Netherlands, 1997.

Ramanathan, V., Crutzen, P. J., Kiehl, J. T., and Rosenfeld, D.: Aerosols, climate, and the hydrological cycle, Science, 294, 2119–2124, 2001.

Seinfeld, J., Pandis, S.: Atmospheric Chemistry and Physics John Wiley, 1998.

Schauer, J., Kleeman, M. J., Cass, G. R., Simoneit, B. R. T.: Measurements of emmissions from air pollution sources, Environ. Sci. Technol., 35, 1716–1728, 2001.

Twomey, S.: Pollution and planetary albedo, Atmos. Environ., 8, 1251–1256, 1974.

Vali, G.: Quantitative evaluation of experimental results on heterogeneous freezing nucleation of supercooled liquids, J. Atmos. Sci., 29, 402–409, 1971.

Vali, G.: Freezing rate due to heterogeneous nucleation, J. Atmos. Sci., 51, 1843–1856, 1994.

Wallace, J., Hobbs, P.: Atmospheric Science Academic Press, 2006.

Zobrist, B., Koop, T., Luo, B. P., Marcolli, C., and Peter, T.: Heterogeneous ice nucleation rate coefficient of water droplets coated by a nonadecanol monolayer, J. Phys. Chem. A, 111, 2149–2155, 2007.

Zobrist, B., Marcolli, C., Peter, T., and Koop, T.: Heterogeneous ice nucleation in aqueous solutions: the role of water activity, J. Phys. Chem. A, 112, 3965–3975, 2008.